Powder Metallurgy Progress, Vol.18 (2018), No.1, p.001-005
http://dx.doi.org/10.1515/pmp-2018-0001

Obituary – Andrej Šalak

Ing. Andrej Šalak Dr.Sc., one of the most experienced powder metallurgists and in particular a pioneer of ferrous powder metallurgy and sintered steels, passed away on January 6th, 2018, at the age of 93, in his hometown of Košice, Slovakia.

Andrej Šalak was born on October 20th, 1924 in Kamenica nad Cirochou in Eastern Slovakia. His father was just a farmer and ran a small pub, but he was a farsighted man who took care that his sons got as profound an education as possible. Andrej passed primary school and then secondary school at the Gymnasium in Michalovce, graduating in 1944. At the end of World War II, when Eastern Slovakia became a battleground between the German and Soviet Armies, Andrej worked in a factory in Svit, in the Tatra area, and thus avoided to be caught or recruited by any of the armies. After the turmoils of World War II he studied Mechanical Engineering at the Czech Technical University in Prague, graduating there in 1949. Even then, Andrej was a very independent and courageous mind: during the Communist takeover in February 1948, the last public supporters of the democratic government were a group of student demonstrators, and Andrej was among them. Therefore he was first denied graduation and was ordered work in a mine, “to prove his relationship to the working class”. Fortunately, a sympathetic doctor who understood the background declared him physically unfit for mining, and Andrej thus was transferred to a metalworking company, the renowned Škoda. After finally being allowed to graduate, he worked in several companies until joining the Institute of Experimental Metallurgy of the Slovak Academy of Sciences (UEM-SAV, now: Institute of Materials Research) in Košice.

Here Andrej worked on deep drawing of steel sheet, earning his PhD on this topic in 1965, but he also did pioneering work in virtually every field of ferrous powder metallurgy, e.g. powder manufacturing – he tried oil atomization long before such powders were on the market – , induction sintering and sintered alloy steels. In the latter area Andrej thoroughly studied manganese as an alloy element in sintered steels and recognized the high potential of this element for obtaining excellent mechanical properties, also due to its tendency to form lower bainitic microstructures which combine favourable strength and toughness. Andrej also described the peculiar homogenization behavior of Mn during sintering, via a gas phase transport mechanism, as well as the “self-getter” effect caused by the Mn vapour shell generated around the compacts in the course of the sintering process. This specific effect enables sintering in atmospheres that would otherwise be regarded oxidizing to Mn, since the Mn vapour shell prevents oxygen and water vapour from coming in contact with the component itself. These findings were published in numerous articles, also in English journals, and anyone who works on sintered Mn steels should start with reading Andrej Šalak’s publications.

However, despite his excellent performance at UEM-SAV, which made Kosice a strongpoint of powder metallurgy, Andrej was ousted from the institute in 1978 due to political reasons. Political persecution was so severe that Andrej could not even find any other employment in the city of Košice. Andrej was however not intimidated: He approached the management of the ZVL bearing company in Dolny Kubin, North Slovakia, and convinced them that powder forged bearing rings would exhibit load-bearing capacity superior to that of wrought steels and could also be produced more economically.

After getting their consent and funding, he joined ZVL-VURAL, the ZVL research facility in Žilina, and within one year produced the first specimens on the newly established powder forging line. The bearings rings manufactured on Andrej's production line were highly successful; they had about double the lifetime of wrought steel rings at 20% lower cost. Also these results were published and found international recognition, although Andrej was continuously in the focus of the political police, the StB, and was accused of espionage on several occasions when he had contact with Western scientists, as vividly described by his friend Erik Navara in the following obituary. Despite these harassments, Andrej always kept contact with his Western colleagues, and although personal meetings could only take place within Czechoslovakia, there were many fruitful discussions. The undersigned had the pleasure to first meet Andrej Šalak at the Czechoslovak PM Congress in Brno in 1982, through my academic teacher Gerhard Jangg who had been Andrej's friend for a long time. Already at that occasion I was very impressed by Andrej's very precise questions in the discussions following each lecture, where he always hit the crucial items.

After the fall of communism, in 1990, Andrej was rehabilitated. At that time he initiated the acquisition of a small part of ZVL by MIBA from Austria, which developed into what is now MIBA Sinter Slovakia, with about 1200 employees. I.e. Andrej's initiative, which started at a meeting with MIBA representatives at TU Wien in February 1990 that was organized by Gerhard Jangg, resulted in a true success story, both for MIBA and the Northern Slovak region of Dolny Kubin.

After his rehabilitation, Andrej once more joined UEM-SAV in Košice and continued work on sintered steels, cooperating in a NATO project on manganese alloyed steels. He also lived to see Mn steels being the focus of the international project "Höganäs Chair" Round III in which IMV-SAV was participating. In 1997, at the age of 73, he obtained the "big" doctorate, the Dr.sc. (equivalent to the Habilitation in the German-speaking countries) on his favourite topic, manganese alloyed sintered steels. Another topic Andrej focused on was the machining behavior of sintered steel; he could prove that the reason for the poor machinability of sintered steels is not the porosity and the resulting interrupted cut but the densification and resulting work hardening in front of the cutting edge.

Andrej is the author or co-author of more than 450 publications in scientific journals and proceedings and of 33 patents. In 1995 he published his book "Ferrous powder metallurgy", the first monograph on this topic since the "Kieffer-Hotop" of 1948. This was followed by the books "Machinability of Powder Metallurgy Steels" in 2005 and finally "Manganese in Powder Metallurgy Steels" in 2012, at the age of 88 ! Andrej was also active in organizing the Powder Metallurgy Congresses in Czechoslovakia between 1973 and 1992 and, starting from 1996, the International Conferences on Deformation and Fracture in Powder Metallurgy. His international cooperations included scientific institutions e.g. in Germany – formerly also East Germany - , Austria, Great Britain and Bulgaria. Andrej has also been a member of the Advisory Board of "Powder Metallurgy Progress" since the journal was established in 2001.

In 1995 Andrej was awarded the Gold Medal of the Presidium of the Slovak Academy of Sciences for his scientific achievements. In 2004, in the course of the Powder Metallurgy World Congress in Vienna, he received the Distinguished Service Award of the European Powder Metallurgy Association (EPMA), to honour his long and successful career in powder metallurgy..

Andrej is survived by his wife Helena, daughter Marcela and son Zdenko, 2 grandchildren (Marek and Boris) and 4 great-grandchildren. All of us who had the opportunity to meet Andrej and get to know him personally will gratefully remember his profound knowledge in powder metallurgy and precise scientific thinking, which made him an excellent partner for discussions. Furthermore, Andrej had a specific feeling for the practical implications of scientific findings. Today, “innovation”, the transfer of scientific results to industrial practice, is a buzzword and strongly promoted e.g. by the EU, but in that connex Andrej was a true innovator already in the early days. Furthermore, Andrej will be remembered for his kind and open mind and hospitality – he liked to show visitors around his home country of Slovakia and had a profound geographic and historical knowledge - as well as his friendly manner and encouraging way in particular to young and less experienced scientists. Thus he helped ensure that powder metallurgy will make progress also in the future. Andrej Šalak will remain in our memory as a true pioneer of powder metallurgy, as an impressive and independent-minded personality and as a good and reliable friend. We shall miss him!

Herbert Danninger

My personal obituary for Ing. Andrej Salak, Dr.Sc.

I have known Dr. Salak since the time he joined our small team of scientists at the recently established Institute of Metallurgical Technology in Kosice. It was in early sixties of the past century and much of the research was oriented toward powder metallurgy.

Soon we became very close friends, much more than simply colleagues at the Institute. In addition to our devotion to research, we shared mutual interest in out-door activities all year round, i.e. going for outings to beautiful natural environments in Eastern Slovakia, bathing in lakes, mushroom picking in summer and skiing trips in winter. We used to discuss all possible topics, ranging from science to politics and what the future would bring. When I recall that period of our lives, I know that we both felt that the times we lived in were unusual, to put it mildly, and that some change was imminent.

At the start of the year 1968 I left the Institute as I was invited to Chalmers University of Technology in Gothenburg, Sweden, as visiting scientist. This position was meant as temporary, however, because of the invasion of our country by Warsaw treaty armies, followed by the Soviet occupation, I chose to remain in Sweden and changed my status of visiting scientist to doctoral student.

Even in those days I remained in correspondence touch with Dr. Salak. In early seventies his friendship became invaluable to me. I applied for being allowed permanent residence abroad (such were the conditions in the communist era) and for that I was in need of a person who would represent me in dealings with several authorities, some of which were pretty hostile. Dr. Salak obliged me and took on himself to act in my cause. His service was of utmost importance to me and, after months of dealings and actions, the outcome was successful.

We could then meet again in person and resume our research co-operation. In late seventies Dr. Salak informed me of his achievements related to sintering iron powder mixed with manganese, or ferromanganese powder. As a result of that we kept exchanging ideas and complementing each other in research. Salak made use of the very high partial pressure of manganese gas at the usual sintering temperatures and proved that manganese can diffuse into iron even when the oxygen potential of the sintering atmosphere lies above the Mn-line in the Ellingham diagram. I contributed to Salak’s research with two papers, presented at two powder metallurgy symposia. Both papers confirmed and, to some extent elucidated Salak’s research results.

Writing about our co-operation in research in the eighties of the last century brings back memory of an incident, typical of the times we lived in. My colleague in Sweden, Professor K. Easterling, attended a scientific conference in Slovakia. He had been well informed of Dr. Salak and of our co-operation. Salak used this opportunity and gave Easterling a couple of metallographic samples for the purpose of having them investigated, I think using surface microanalytical methods, for which we had facilities at that time missing in Kosice. The passing of the samples was noticed by some person, connected with that-time secret state police and, consequently, the samples were confiscated at an unexpected check of Easterling’s suitcase at the airport. Few weeks later, Salak was called for questioning, a very unpleasant experience in the communist days. However, after the samples had been investigated at some laboratory, the preposterous “espionage” charges were dropped, to the relief of all of us involved in the incident, and did not stop our continued co-operation.

In 1987 I left Sweden for Zimbabwe and my research interests changed. However, we kept in touch and when e-mail became available our correspondence multiplied. I was informed of his research activities, leading to the D.Sc. degree and to the publication of his two books.

Dr. Salak will be remembered by me and by all his colleagues and members of the scientific community for his many qualities: a top-class scientist, a dedicated researcher, a true friend of all who worked with him and shared his broad interests.

I, personally, will miss you very much, dear Andrej. May you rest in peace.

In Jihlava, Czechia, January 12, 2018.
Erik Navara, retired professor of Physical Metallurgy

Powder Metallurgy Progress, Vol.18 (2018), No.1, p.006-020
http://dx.doi.org/10.1515/pmp-2018-0002

THE ROLE OF THE ATMOSPHERE ON BORON-ACTIVATED SINTERING OF FERROUS POWDER COMPACTS

V. Vassileva, H. Danninger, S. Strobl, Ch. Gierl-Mayer, R. de Oro Calderon, H. Hutter

Abstract

Boron has been known to activate densification during sintering of ferrous powder compacts, though with risk of embrittlement. In the present study, specimens Fe-B and Fe-C-B prepared from standard atomized iron powder with addition of ferroboron Fe-21%B were sintered in different atmospheres, and the resulting microstructures and properties were studied. It showed that the activating effect of boron is observed during sintering in argon and in hydrogen while sintering in N_2 containing atmospheres results in rapid deactivation of boron, through formation of stable BN. In hydrogen atmosphere, surface deboronizing was observed to considerable depth. Ar is chemically inert, but Ar trapped inside closed pores tends to inhibit further densification. The impact energy data indicated that the embrittling effect of boron is enhanced significantly by presence of carbon. In the fracture surfaces, transgranular cleavage fracture can be observed both at very low and high impact energy values.

Keywords: Sintered steels, boron, atmosphere, embrittlement

INTRODUCTION

For sintered steels, the density is the single factor that dominates the properties, especially the mechanical ones. High sintered density is therefore a most attractive target, and in addition to compacting techniques, also activating the sintering process is a viable way to increase the sintered density level, at least if shrinkage occurs in a stable way and distortion is avoided. One of the most effective sintering activators is boron, as has been shown already in the 1950s [1]. Boron is virtually insoluble in iron or steel, and it forms a eutectic melt above about 1170°C [2]. In ferrous powder compacts, persistent liquid phase is generated in this temperature range that strongly promotes densification [3].

This effect has been used for sintering of numerous types of PM steels [4-6], also different boron carriers being employed such as elemental boron, ferroboron, or B containing masteralloys [7, 8]. Also hexagonal boron nitride has been used which decomposes in N-free atmospheres [9-11], forming Fe-B liquid phase. On the other hand, however, the very low solubility of B both in austenite and ferrite means that the persistent liquid phase solidifies in situ, and above a given B content a continuous network of boride eutectic remains that results in pronounced embrittlement of the sintered compact, at least in mechanical properties that are significantly inferior to those that could be expected from the density level.

Vassilka Vassileva*, Herbert Danninger, Susanne Strobl, Christian Gierl-Mayer, Raquel de Oro Calderon, Herbert Hutter: Technische Universität Wien, Institut für Chemische Technologien und Analytik, Getreidemarkt 9/164, A-1060 Wien/Vienna, Austria, *now: OMV AG, A-1020 Wien/Vienna, Austria

In [9] it has been shown that for gravity sintered, highly porous stainless steel filters the presence of eutectic boride layers at the sintering contacts is not a problem as long as these eutectic regions are isolated since they are sufficiently strong that during mechanical loading the plastic deformation is shifted to the ductile austenitic base material. If however the eutectic structure is interconnected, i.e. continuous, – and if the matrix itself is only moderately ductile – failure in one location will result in immediate brittle failure along the boride structure. The success of boride activation therefore depends on the concentration of boron available: it has to be chosen at such a level that is sufficiently high to yield the desired activation, i.e. densification; on the other hand it should be sufficiently low that only local boride eutectic remains and formation of interconnected areas is precluded. This "concentration window" is reportedly rather narrow, and it can be assumed that it is also defined by the presence of alloy elements such as carbon or Mo [12, 13]. Also other elements such as Ni [8] or Mn [14] have been shown to affect the microstructure and thus the mechanical properties. Furthermore, boron is known to react with constituents of the sintering atmosphere such as hydrogen to form volatile compounds [15, 16], and it is also a strong nitride former. As stated above, hexagonal boron nitride admixed to steel powder has been shown to decompose during sintering e.g. in vacuum, resulting in boron activation, but on the other hand also the reverse reaction, i.e. reaction of boron with N_2 from the atmosphere, with subsequent formation of inert hBN, can be expected, as has been shown e.g. by Momeni [10].

In this work, the sintering behaviour of ferrous compacts containing varying amounts of boron was studied in different atmospheres, both plain Fe and Fe-C matrices being employed.

EXPERIMENTAL TECHNIQUE

The base powder used was plain iron powder ASC 100.29 (Höganäs AB); in part natural graphite UF4 (Kropfmuehl) was admixed. Boron was introduced as ferroboron powder (Fe-21 mass%B) supplied by IMR Kosice. This powder was mostly fine (<45 μm) but contained some coarser fractions that were not screened off but were retained as markers for liquid phase formation, coarse secondary pores indicating that liquid phase has been generated during sintering (see below), which however did not affect the distribution of the liquid phase 0.5 mass% EBS (Microwax C) was added as pressing lubricant. The powders were dry blended for 60 min in a tumbling mixer and uniaxially compacted in a tool with floating die to standard impact test bars (ISO 5754) 55 x 10 x ca. 8 mm^3. The compacting pressure was uniformly 600 MPa. Dewaxing was performed separately prior to sintering in a tube furnace in flowing N_2 of 99.999% purity (5.0 grade) for 30 min at 600°C. Sintering in high purity (5.0 grade) N_2 and Ar, respectively, was done in a pushtype furnace heated by SiC rods that was equipped with a gas tight Kanthal APM superalloy muffle, consistently high purity of the atmosphere being thus established. Sintering in H_2 was done in a pusher furnace Degussa "Baby" with Mo heating elements; here sintering of the carbon-containing specimens was done in getter boxes using Al_2O_3 - 5% graphite as getter. In part sintering was performed in parallel at 1200°C and 1300°C, respectively, to study the effect of the varying liquid phase content. Isothermal sintering time was uniformly 60 min. Cooling was done by pushing the boats / getter boxes into the water-jacketed exit zones of the furnaces.

Characterization of the specimens was done following standard techniques: The green density was determined from the mass and dimensions while the sintered density was measured through water displacement; here, the specimens were impregnated before measurement using a commercial waterstop spray, to avoid intrusion of water into open pores. Mechanical testing included Vickers hardness and Charpy impact energy on unnotched samples, since it has been found that hardness and impact energy are markedly better suited to describe the mechanical behaviour of sintered steels than the usual combination of R_m and A, in particular at low to moderate ductility levels. In all cases, metallographic investigations were performed, 2% Nital (MeOH-2%HNO_3) being used as etchant. The boron distribution was studied in metallographic sections by secondary ion mass spectrometry (SIMS CAMECA 3f, primary ions Cs^+ at 15.5 keV energy, 150 nA current).

RESULTS

Results obtained with Fe-B materials

In Figure 1 the properties obtained when sintering Fe-x%B in flowing high purity argon are shown. Ar was used here since it can be regarded as a chemically inert atmosphere. As can be seen in Fig.1, the green density slightly drops with increasing B content – due to the adverse effect of the admixed hard ferroboron on the compressibility – while the sintered density increases significantly as a consequence of B addition. Sintering at 1300°C is more effective than at 1200°C, but this holds – not surprisingly - also for the reference materials without B. Typically the density increases as a function of the B content only up to about 0.15 to 0.20% and then levels off, in particular when sintering at 1300°C. This effect can be attributed to trapping of the argon in the pores: since Ar is completely insoluble in iron even at high temperatures, pores filled with Ar remain so when the pore morphology changes from open to closed one, and if the pore shrinks due to capillary forces, the internal pressure increases, opposing further densification. This "argon trapping" effect is the reason why materials routinely to be sintered to full density – heavy alloys, hardmetals, tool steels – are never sintered in argon.

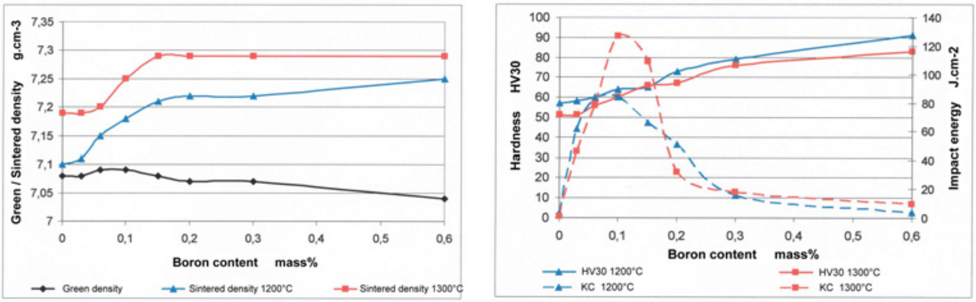

a) Density of Fe-x%B b) Hardness and impact energy

Fig.1. Properties of Fe-x%B sintered in Ar 99.999 as a function of the B content. Fe-21B, compacted at 600 MPa, sintered 60 min isothermal.

When observing the mechanical properties it can be stated that the hardness increases consistently with increasing B content while for the impact energy typical "windows" of optimum B content are discernible, as could be expected from the facts described above. The window is slightly narrower for 1300°C sintering temperature than for 1200°C, indicating that at 1300°C the critical liquid phase content – that results in continuous boride networks after sintering – is obtained at lower B contents than at 1200°C. Nevertheless, the impact energy values obtained are quite impressive - >100 $J.cm^{-2}$ for

0.10% and 0.15%B when sintering at 1300°C – which indicates that here the desired sintering effect has really been obtained without embrittlement.

The extremely low impact energy values obtained for the plain iron reference materials seem to be surprising at first. However, it has to be kept in mind that high purity plain iron tends to exhibit excessive grain growth during the austenite-ferrite transformation [17], which effect is particularly pronounced with sintered plain iron [17-19]. As shown e.g. in [18, 20], those extremely coarse-grained specimens are prone to brittle intergranular fracture, with impact energy values < 5 J.

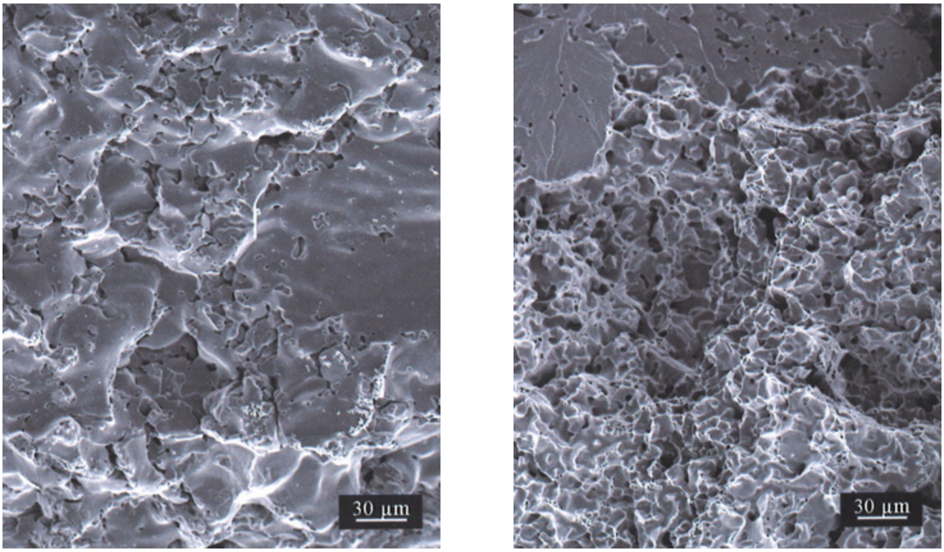

a) Plain Fe b) Fe-0.06%B

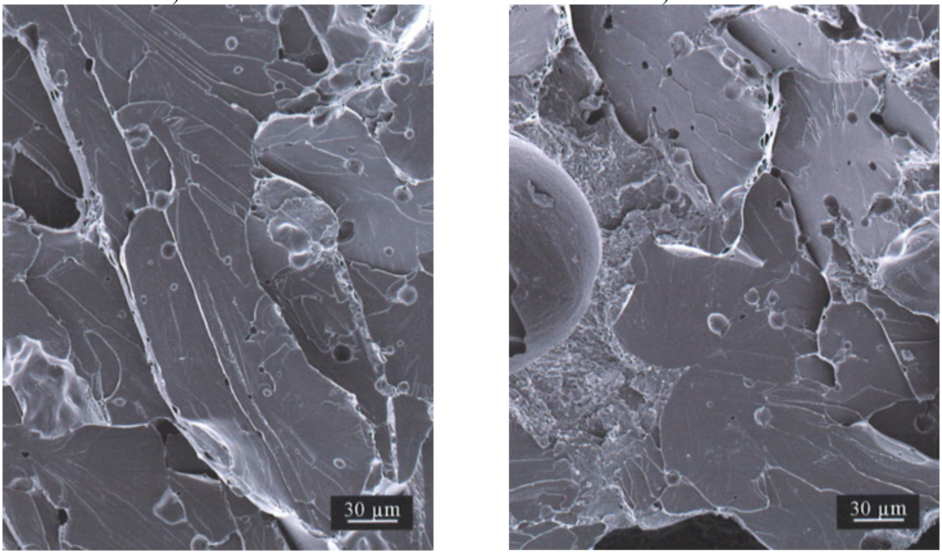

c) Fe-0.15%B d) Fe-0.30%B

Fig.2. Fracture surfaces of Fe-x%B, sintered 60 min at 1300°C in Ar. Ferroboron Fe-21B.

The effect can clearly be seen in the fracture surfaces. In figure 2, typical impact fracture surfaces are shown. Here, for the plain iron specimen the typical smooth surface of the intergranular failure can be seen (Fig.2a). At moderate B levels <0.15%B the grain coarsening is already suppressed, and mostly ductile rupture is obtained, localized cleavage being discernible (Fig.2b). This effect of interstitials has also been observed with H, C and N; in the present case also B_2O_3 traces might slow down grain growth, although the fairly high vapour pressure of this oxide renders marked effects rather improbable. Surprisingly, the high impact energy specimens Fe-0.15%B and the rather brittle Fe-0.3%B exhibit almost the same fracture mode, in both cases transgranular cleavage being observed (Fig.2c, d). This confirms the fact observed also e.g. with W heavy alloys [21] that the appearance of cleavage facets does not necessarily mean macroscopically brittle failure since there may have been considerable plastic deformation before cleavage occurs. On the other hand, comparison with standard fine grained sintered iron specimens (see e.g. [22,23]) indicates that boron enhances cleavage fracture, suppressing the ductile rupture typical for these materials.

Sintering the same compact grades in H_2 results in markedly different properties (Fig.3). Here, densification is fairly consistent right up to 0.3%B, then the density drops. As metallographic sections have shown, there is some effect of internal gas formation which at high B levels, when the pores are closed in an early stage of sintering, tends to stabilize the pores, although real blistering was not observed.

The relationship hardness-boron content is similar as in the case of Ar, consistently higher hardness being attained with higher boron levels. On the other hand, the impact energy of the plain iron reference specimens is drastically higher than after sintering in Ar, since there is pronouncedly less grain growth, and the level of interfacial oxygen is reduced [18]. Also here there is a positive effect of B on the impact energy that is more pronounced at 1300°C sintering temperature than at 1200°C, and – at first surprisingly – also extends to higher B levels, which disagrees with the results obtained when sintering in Ar.

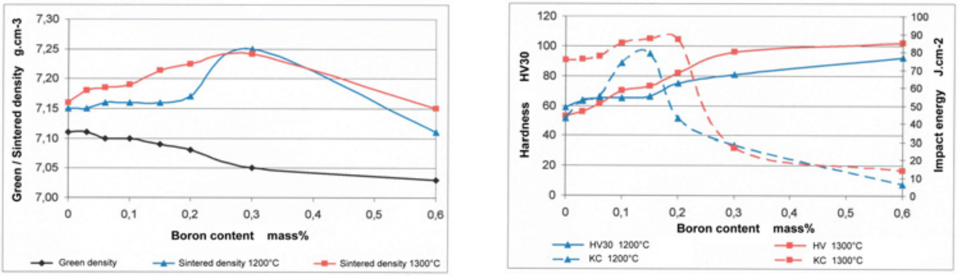

a) Density of Fe-x%B b) Hardness and impact energy

Fig.3. Properties of Fe-x%B sintered in H_2. as a function of the B content. Fe-21B, compacted at 600 MPa, sintered 60 min isothermal.

The reason for this disagreement can at least in part be attributed to the interaction between B and H_2. As was shown by metallographic investigations, there is considerable deboronizing of the specimens in particular at and near the surfaces (Fig.4), clearly indicated by the absence of the characteristic boride network. The deboronized areas are ductile, since there is no embrittling phase; however, ductile areas are found also in the cores at moderate boron levels as visible from the fracture surfaces; compare Fig.5c and Fig.2c, depicting specimens with the same nominal B content. In figure 5c, both cleavage and pronounced ductile failure stand out clearly. As shown in [16], almost complete deboronizing can be obtained through very long isothermal sintering in hydrogen atmosphere. This results in an almost fully dense and highly ductile material; unfortunately, however, the times necessary render such a process very uneconomical and thus not suitable for industrial practice. In the fracture surfaces also the coarsening of the microstructure caused by persistent iron-boron liquid phase can be seen, which contributes to the loss of ductility at higher B levels.

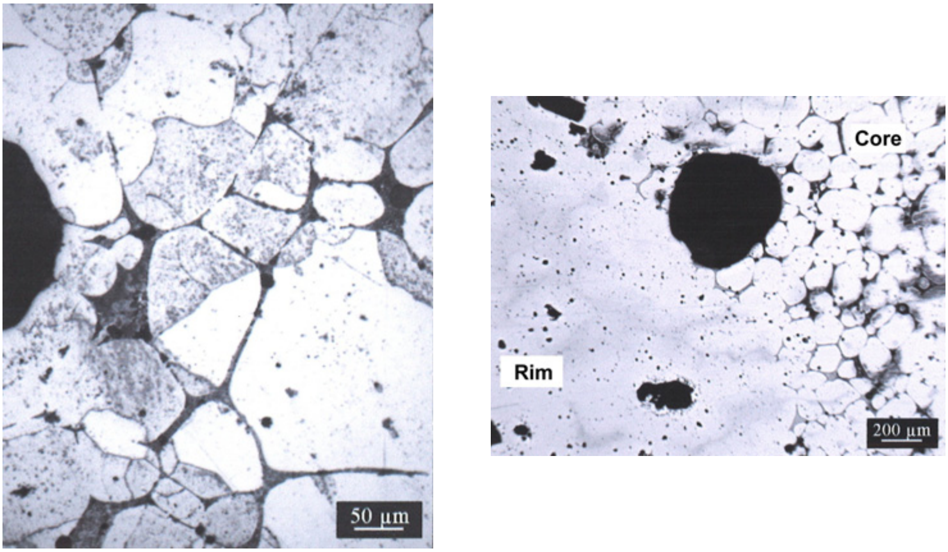

a) Fe-0.3%B

b) Fe-0.6%B, Metallographic section, near surface

Fig.4. Metallographic sections of Fe-x%B, sintered 60 min at 1300°C in H_2.

Sintering in N_2, finally, does no exhibit any signals for B activation: there is neither a significant effect on the density nor on the impact energy – in positive or negative direction. As visible from Fig.6a, the sintered density follows quite the same trend as the green density, simply at a slightly higher level. Hardness and impact energy show a similar behaviour; also there neither the significant enhancement of the impact energy at moderate B contents nor the drop of of this property as a consequence of boride embrittlement is found. This clearly indicates that boron has been deactivated by reaction with the atmosphere. This is also clearly visible from the metallographic section in Fig.7: compared e.g. with Fig.4a the microstructure does not show any traces of liquid phase sintering, and also the coarse ferroboron particles were not dissolved, leaving secondary pores, as shown in Fig.4a, but remained in place, indicating that the boron they contained was no more available to form liquid phase. Also the fracture surfaces resemble those of plain sintered iron (Fig.8).

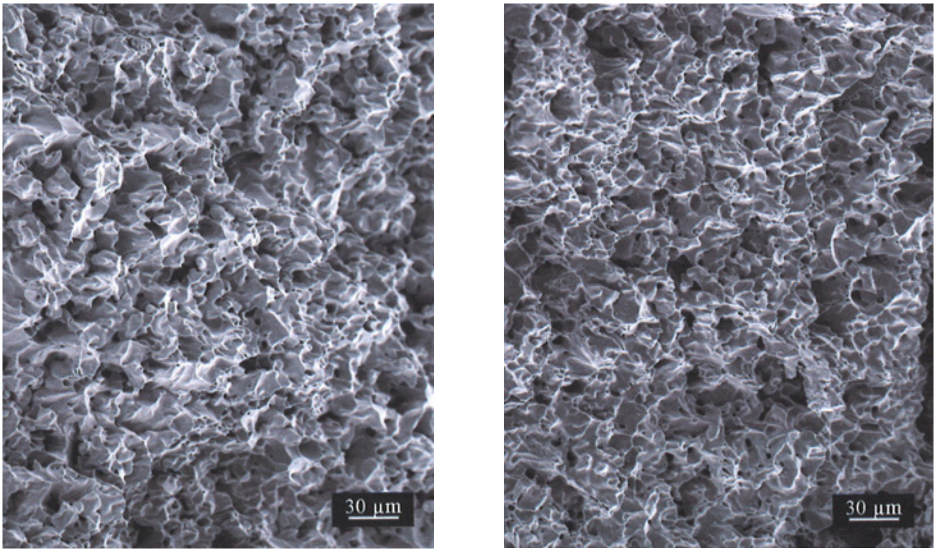

a) plain Fe b) Fe-0.06%B

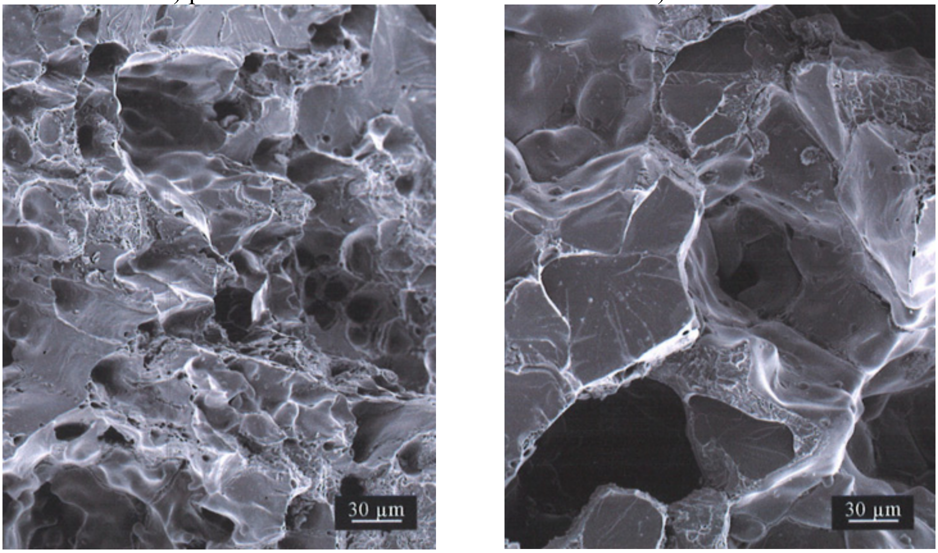

c) Fe-0.15%B d) Fe-0.30%B

Fig.5. Fracture surfaces of Fe-x%B, sintered 60 min at 1300°C in H_2. Ferroboron Fe-21B.

On metallographic sections, the boron distribution was analyzed through secondary ion mass spectrometry (SIMS). This technique is particularly suited for light elements that are difficult to analyze e.g. by SEM-EDS, boron being particularly tricky. The elemental mappings are shown in Fig.9.

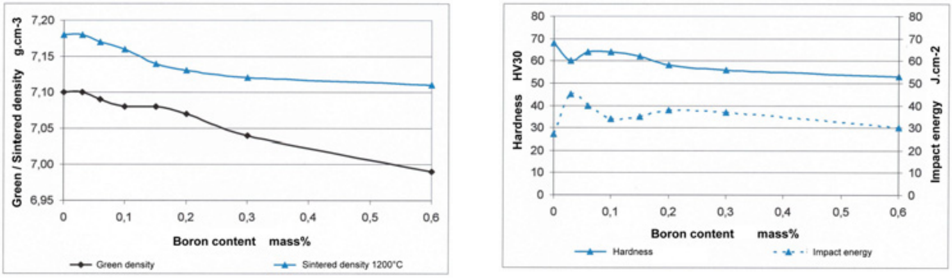

a) Density of Fe-x%B b) Hardness and impact energy

Fig.6. Properties of Fe-x%B sintered in N_2. Fe-21B, compacted at 600 MPa, sintered 60 min isothermal.

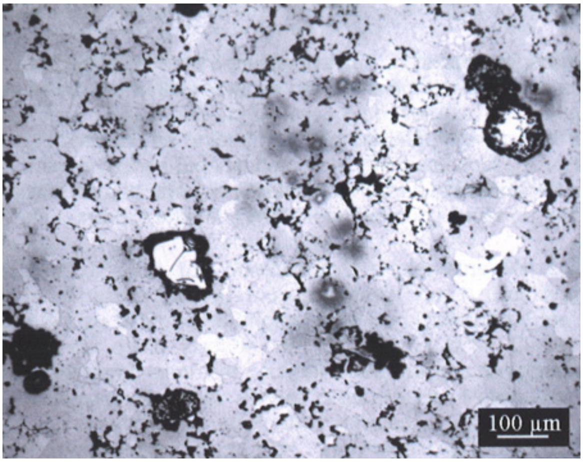

Fig.7. Metallographic section of Fe-0.2%B, sintered 60 min at 1200°C in N_2.

As can be clearly seen, for all boron contents studied the B distribution in specimens sintered in Ar and H_2, respectively, is relatively similar. Evidently the boron phases are isolated at 0.06% and 0.15%B while at 0.30%B continuous networks are visible. This agrees with the impact energy data which show that at 0.15%B fairliy high impact energy is measured while at 0.30%B brittle fracture, with low IE data, are obtained. This once more confirms that the main problem of B activation is the formation of interconnected boride networks that embrittle the materials, although, as visible e.g. in Fig.2c, d and 5d, fracture does not occur in the typical intergranular manner known e.g. from P alloyed sintered steels [24]. In the case of sintering in N_2 none such network is observed, which confirms that liquid phase is not formed here since boron is deactivated by BN formation [10] and remains localized at the sites of the original ferroboron particles (Fig.7).

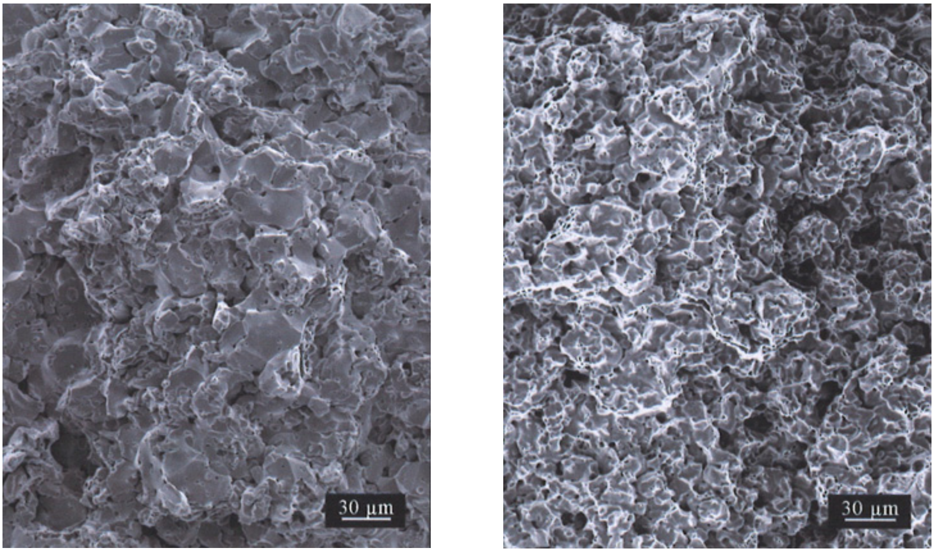

a) 0.00%B b) 0.06%B

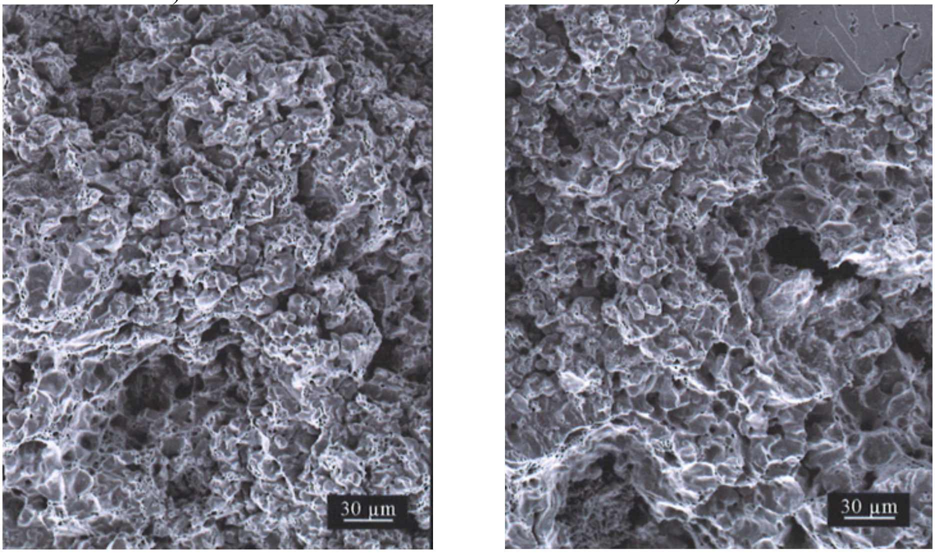

c) 0.15%B d) 0.30%B

Fig 8. Fracture surfaces of Fe-x%B, sintered 60 min at 1300°C in N_2. Ferroboron Fe-21B.

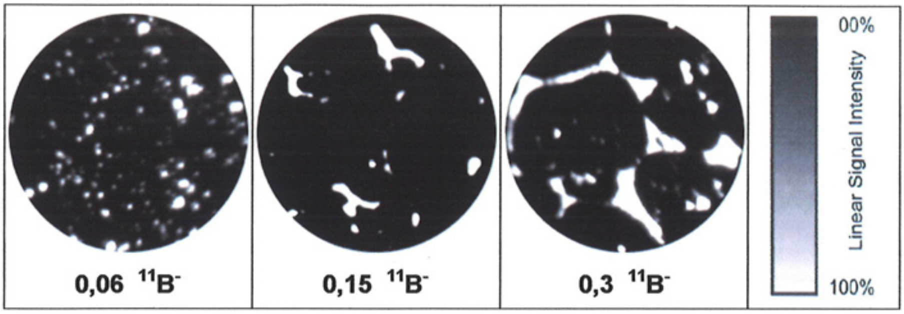

a) Argon

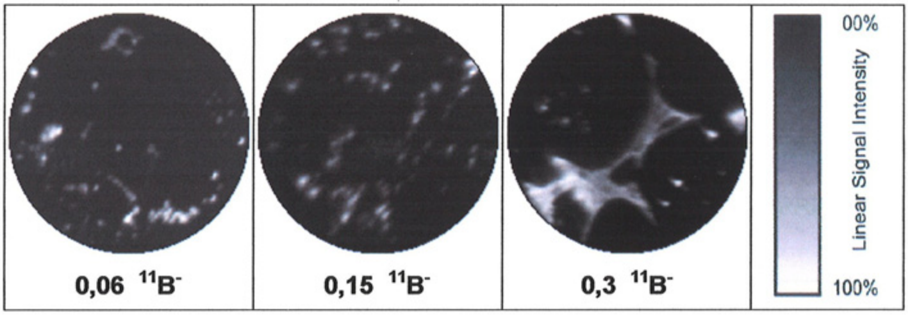

b) Hydrogen

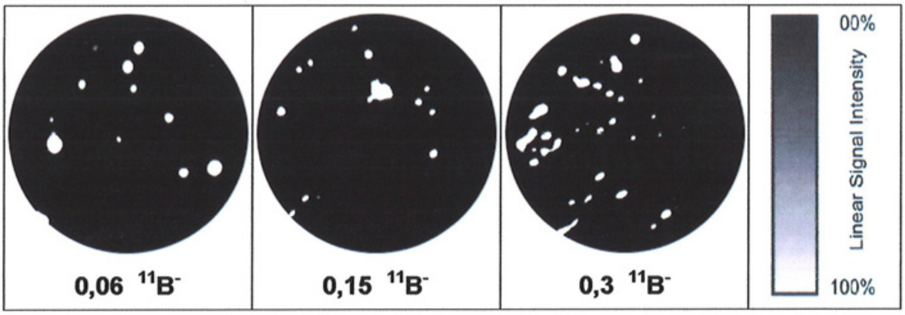

c) Nitrogen

Fig.9. Qualitative SIMS boron mappings of Fe – x%B, compacted at 600 MPa, sintered 60 min 1200°C in different atmospheres (99.999% purity). Image diameter 150 um, Cs^+ ions. Scanned area 300x300 μm^2.

Sintered steels containing boron and carbon

Similar experiments were carried out with materials to which 0.8%C had been admixed as natural graphite. The results obtained by sintering in Ar – as the most inert atmosphere used - are shown in Fig.10.

Here it is evident that apparently the results are basically similar to those obtained without C (see Fig.1) but the trends of the graphs are shifted towards lower B contents. This holds in particular for the impact energy: the drop of the values occurs already at very low

B levels: in fact the Fe-C reference material exhibits the best impact energy, and even when admixing only 0.03%B, the impact energy drops below 10 J.cm^{-2}. Similar effects were observed after sintering in H_2, although here the drop of the impact energy was not quite as pronounced, surely in part as a consequence of the deboronizing effect described above. In any case, the activating effect of boron seems to be still less controllable in carbon containing steels than it is in Fe-B.

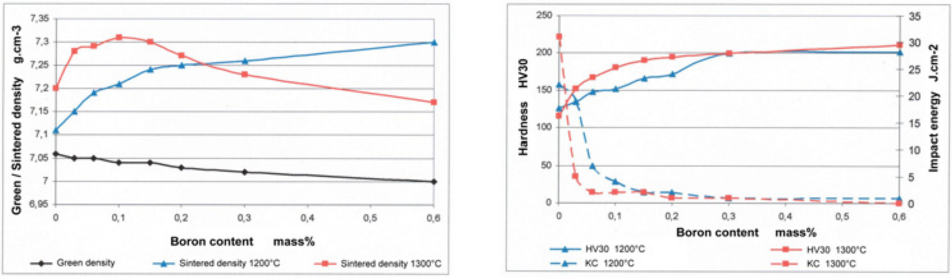

a) Density of Fe-0.8%C-x%B

b) Hardness and impact energy

Fig.10. Properties of Fe-0.8%C-x%B sintered in **Ar** as a function of the B content. Fe-21B, compacted at 600 MPa, sintered 60 min isothermal.

When studying the fracture surfaces (Fig.11) it is evident that the tendency to grain coarsening as well as cleavage fracture is more pronounced than with the carbon-free materials; even at as low B contents as 0.06%, coarse microstructure and almost exclusively transgranular fracture are observed (see Fig.11b). Surprisingly, despite the presence of the continuous boride network (see Fig.11d), integranular fracture is not visible even at higher B levels at which the impact energy values are negligible. This disagreement between microstructure and fracture behaviour has to be investigated further.

For those materials sintered in H_2 (Fig.12), a similar trend is observed, although there is a markedly more pronounced effect of the sintering temperature: At 1300°C, at low to moderate B contents markedly more pronounced densification occurs than at 1200°C, but the impact energy drops even at very low boron contents while after sintering at 1200°C, up to 0.15%B acceptable impact energy data are measured, although also here, as in case of sintering in Ar, the best impact energy values are obtained without any B addition. This once more confirms that the combination of C and B has to be handled with extreme care to obtain acceptable mechanical properties. Furthermore, the coincidence between density and impact energy stands out clearly, indicating that densification by itself is not as relevant as is the strengthening of the individual sintering contacts [25].

In case of Fe-C-B, the deboronlizing effect of the H_2 atmosphere stands out very clearly also in the etched section: as shown in Fig.13, there is a clear difference between the core and the rim areas. The former is significantly coarser, as a consequence of the boron activation, while in the near-surface region, to a depth of about 500 um, a fine microstructure as typical for sintered Fe-C can be seen. This indicates that the activating effect of B has not been present here, as a consequence of boron removal through formation of volatile B_2H_6.

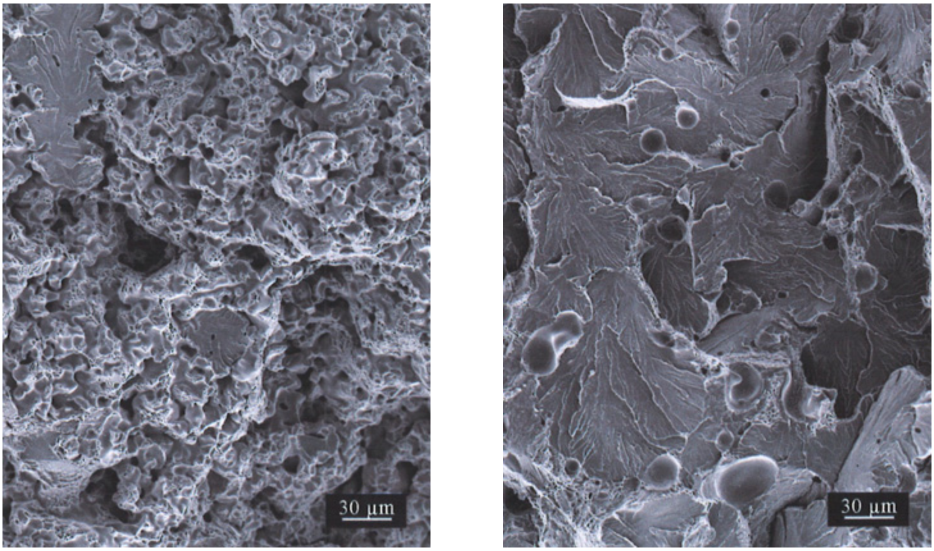

a) Fe-0.8%C b) Fe-0.8%C-0.06%B

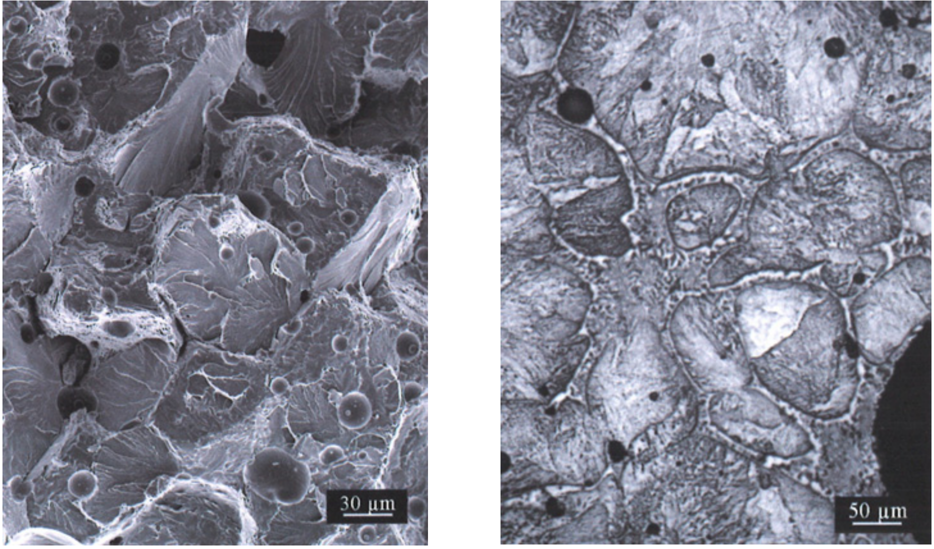

c) Fe-0.8%C-0.3%B d) as Fig.11c; metallographic section

Fig.11. Fracture surfaces of Fe-0.8%C-x%B sintered at 1300°C in Ar.

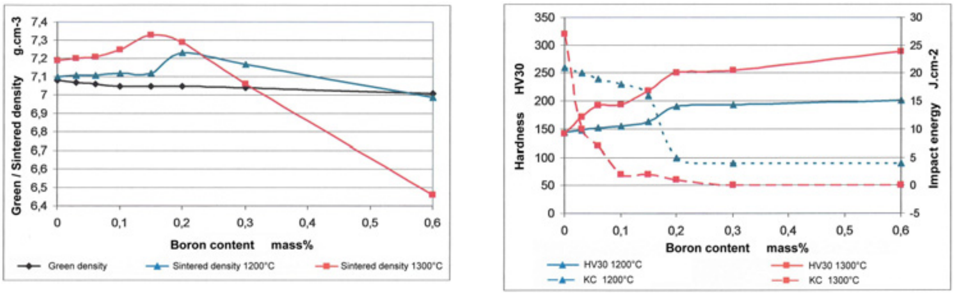

a) Density of Fe-0.8%C-x%B b) HV and impact energy

Fig.12. Properties of Fe-0.8%C-x%B sintered in H_2 as a function of the B content. Fe-21B, compacted at 600 MPa, sintered 60 min isothermal.

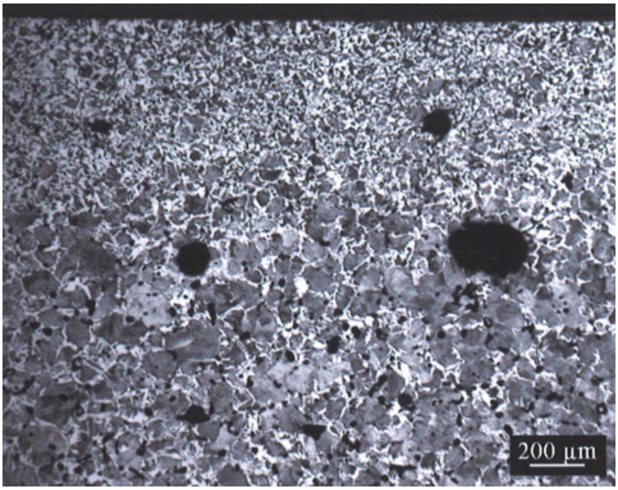

Fig.13. Fe-0.8%C-0.3%B, sintered 60 min at 1300°C in H_2, Nital etched.

The main difference between Fe-B and Fe-C-B is the markedly lower critical B content above which embrittlement occurs. Thermodynamic calculations using the software ThermoCalc were carried out with both systems. They have shown that the combination of B and C in steels results in considerable lowering of the solidus temperature (Fig.14a): this means that on one hand the liquid phase is formed at lower temperature, and on the other hand at a given temperature more liquid phase is formed in case of Fe-B-C than in case of Fe-B, as also indicated in Fig.14b which shows the phase content as a function of the temperature. This can be taken as an indicator that the more severe embrittlement observed with Fe-B-C might be the consequence of the larger volume fraction of liquid phase at the sintering temperatures chosen here and therefore more brittle phase after sintering, the interconnected boride network being formed already at lower B levels than without carbon. In this case, adapting the sintering conditions would be a measure to at least reduce the embrittlement. However, this has to be corroborated by further experimental work, e.g. thermoanalytical studies as well as mechanical testing, and will be the subject of another publication.

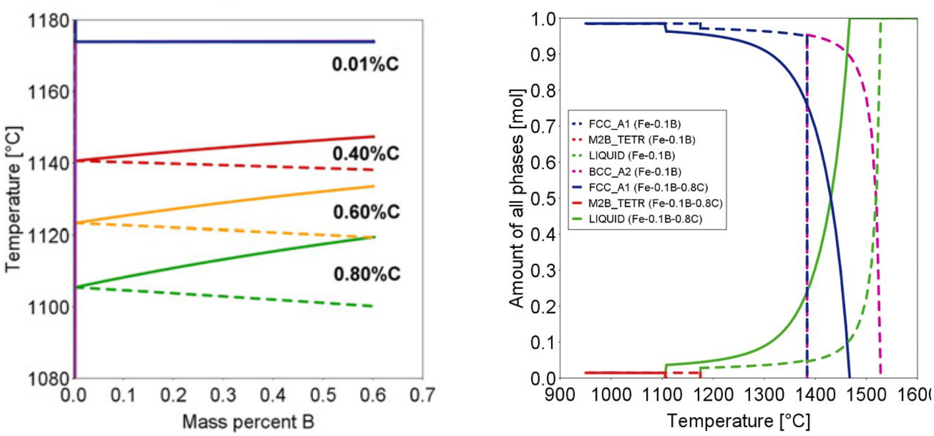

a) Solidus lines in Fe-x%B at different C contents (broken lines: boundary to L+fcc+M2B; solid lines: boundary to L+fcc)

b). Amount of phases in Fe-0.1%B and Fe-0.1%B-0.8%C

Fig.14. Calculated polythermal phase diagrams of Fe-x%B-C.

CONCLUSIONS

In the present study it is shown that sintering of Fe-B with varying B contents in Ar and in H_2 results in the well known activating effect of boron, i.e. in densification and in higher hardness and, at low to moderate B levels, also improved impact energy. At higher B contents the densification effect tends to level off when sintering in Ar, apparently due to the inhibiting effect of Ar trapped in closed pores. The impact energy decreases as a consequence of the formation of brittle boride networks, as clearly visible from SIMS analysis. Surprisingly, even in case of Fe-B materials that show very high impact energy, cleavage fracture dominates, underlining that transgranular cleavage does not necessarily implicate macroscopically brittle behaviour. On the other hand, also the brittle materials fail in a transgranular way and not through plain intergranular fracture as would be expected from a brittle network structure. In H_2, deboronizing occurs, in particular at higher sintering temperatures, resulting in lower B levels than nominal and in less tendency to embrittlement, although the B content thus is still less controllable. Nitrogen deactivates the boron, and the sintering behaviour and properties are similar to those of plain iron.

Addition of 0.8%C increases the tendency to embrittlement. Even B contents <0.1%, which in Fe-B are beneficial, lead to very low impact energy values. In general, the activation of sintering by boron is reasonably controllable in carbon-free materials while in the case of Fe-C-B the “window” for “useful” boron contents – those that are effective towards activation of sintering while still avoiding embrittlement - is narrow and very difficult to control, esp. when regarding the reactivity of B with atmospheric constituents.

Acknowledgement

This work was financially supported by the Austrian Fonds zur Förderung der wissenschaft-lichen Forschung (FWF project no.14889). Furthermore, the assistance and advice of A.Šalak, M.Selecká and E.Dudrová, IMR Kosice, are gratefully acknowledged.

REFERENCES

[1] Benesovsky, F., Hotop, W., Frehn, F.: Planseeberichte Pulvermet., vol. 3, 1955, p. 57
[2] Okamoto, H.: Phase Diagrams of Binary Iron Alloys. Materials Park OH : ASM, 1993
[3] Madan, DS., German, RM., James, WB.: Progress in Powder Metall., vol. 42, 1986, p. 267
[4] Dudrova, E. et al.: Kovove Materialy, vol. 5, 1995, p. 95
[5] Selecká, M., Šalak, A., Danninger, H.: J.Mater.Process.Technol., vol. 143-144, 2003, p. 910
[6] Molinari, A., Straffelini, G., Pieczonka, T., Kazior, J.: Int. J. Powder Metall., vol. 34, 1998, p. 21
[7] Orth, P., Danninger, H., Bouvier, A., Ratzi, R. In: Proc. PM2004 Powder Metallurgy World Congress, Vienna. Eds. H. Danninger, R. Ratzi. Vol. 3. Shrewsbury : EPMA, 2004, p. 307
[8] Gierl-Mayer, C., Zbiral, J., Danninger, H., Ratzi, R. In: Proc. Euro PM2014, Salzburg. Shrewsbury : EPMA, 2014, Paper-Nr. EP14066
[9] Danninger, H., Jangg, G., Giahi, M.: Z.Werkstofftechnik, vol. 19, 1988, p. 205
[10] Momeni, M., Gierl, C., Danninger, H., Avakemian, A.: Powder Metall., vol. 55, 2012, no. 1, p. 54
[11] Momeni, M., Gierl, C., Danninger, H., Ul Mohsin, I., Arvand, A.: Powder Metall., vol. 55, 2012, no. 3, p. 212
[12] Liu, J., Cardamone, A., Potter, TJ., German, RM., Semel, FJ.: Powder Metall., vol. 43, 2000, no. 1, p. 57
[13] Liu, J., German, RM., Cardamone, A., Potter, T., Semel, FJ.: Int. J. Powder Metall., vol. 37, 2001, no. 5, p. 39
[14] Tojal, C., Gomez-Acebo, T., Castro, F.: Mat.Sci.Forum, vol. 534-536, 2007, p. 661
[15] Selecká, M., Bureš, R. In: Proc. Conf. Metallography 1998, IMR Kosice, p. 122
[16] Gierl, C.: PhD thesis. Wien : TU, 1999
[17] Lehr, P.: C.R.Acad.Sci.France, vol. 242, 1956, p. 1172
[18] Danninger, H.: Powder Metall. Progress, vol. 3, 2003, p. 75
[19] Kuroki, H., Suzuki, HY.: Mater. Transactions, vol. 47, 2006, p. 2449
[20] Jaliliziyaeian, M., Gierl, C., Danninger, H. In: Proc. EuroPM2007, Toulouse. Vol. 3. Shrewsbury : EPMA, 2007, p. 131
[21] Danninger, H., Schreiner, M., Jangg , G., Lux, B.: Pract. Metallography, vol. 20, 1983, p. 64
[22] Šlesar, M., Dudrová, E., Parilak, L., Besterci, M., Rudnayová, E.: Sci. Sintering, vol. 19, 1987, p. 17
[23] Danninger, H., Jangg, G., Weiss, B., Stickler, R.: Powder Metall. Int., vol. 25, 1993, no. 4, p. 170; vol. 25, 1993, no. 5, p. 219
[24] Vassileva, V., Krecar, D., Tomastik, C., Gierl-Mayer, C., Hutter, H., Danninger, H.: Powder Metall. Progress, vol. 15, 2015, no. 1, p. 369
[25] Danninger, H., Sonntag, U., Kuhnert, B., Ratzi, R.: Pract.Metallography, vol. 39, 2002, no. 8, p. 414

Powder Metallurgy Progress, Vol.18 (2018), No.1, p.021-030
http://dx.doi.org/10.1515/pmp-2018-0003

SURFACE HARDENING VS. SURFACE EMBRITTLEMENT IN CARBURIZING OF POROUS STEELS

S. Tesfaye Mekonone, I. Cristofolini, W. Pahl, A. Molinari

Abstract

Carburizing increases the contact fatigue resistance of sintered steels, but the surface hardening may result the formation of surface brittle cracks due to the combined effect of high hardness and porosity. The effect of carburizing on the embrittlement of the case of a 7.3 g/cm^3 1.5%Mo - 0.25%C sintered steel was studied. The phenomenon was analyzed theoretically and verified by experiments. The resistance of the carburized steel to surface brittle cracking increases with the load bearing surface and the decrease of the maximum pore size, of the surface microhardness and the friction coefficient. The theoretical analysis was implemented in a design procedure for parts subject to contact stresses.

Keywords: Carburizing, rolling-sliding, hardening; brittleness; design

INTRODUCTION

In lubricated rolling and rolling-sliding contacts, the main damage mechanism is contact fatigue that occurs through the nucleation of a subsurface crack, its propagation towards the surface and the formation of metallic debris. The resistance of porous sintered steels to this damage mechanism has been investigated in previous works, proposing a theoretical model to predict the nucleation of the subsurface crack [1-2]. The model is based on a conservative approach, starting from the assumption that crack nucleation is anticipated by local plastic deformation [3]. Therefore, if the resistance to plastic deformation of the matrix is higher than the maximum local stress, no plastic deformation occurs and, in turn, subsurface cracks do not nucleate.

The resistance to plastic deformation of the matrix σ_{yo} can be calculated from microhardness HV by eq. (1) [4], while the maximum local stress σ can be calculated from the equivalent stress σ_{eq} by eq. (2) [5].

$$\sigma_{yo} = \frac{HV}{4.2} \tag{1}$$

$$\sigma = \frac{\sigma_{eq}\beta_k}{\phi} \tag{2}$$

where β_k is the notch effect coefficient (2.4 for heat treated steels [6]) and Φ is the fraction of the load bearing section that may be determined from the fractional porosity and its morphology [7]. A detailed description of the theoretical model is reported in [2].

S. Tesfaye Mekonone, Ilaria Cristofolini, Alberto Molinari, University of Trento, Trento - Italy
Wolfgang Pahl, GKN SinterMetals, Brunico (BZ) - Italy

Figure 1 shows, as an example, a graphical representation of this model in case of a through hardened steel. It compares the yield strength of the matrix corresponding to different microhardness levels to the maximum stress profile corresponding to different fraction of the load bearing section, in specific contact conditions (curvature radii of the counteracting parts, contact length, contact force), just to highlight the influence of the microstructural characteristics of the sintered steel.

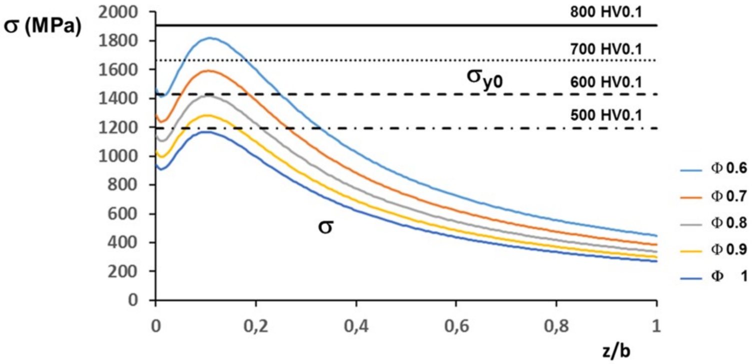

Fig.1. Yield strength of the matrix and maximum stress profile highlighting the conditions that cause subsurface plastic deformation.

For any fraction of the load bearing section, there is a minimum microhardness to avoid the nucleation of the subsurface crack. On decreasing the fraction of the load bearing section, the matrix microhardness has to be increased. This leads to a highly risky situation, since it has been demonstrated that pores may act as pre-existing cracks above a microhardness threshold, promoting brittle behavior [8].

Carburizing is a thermochemical treatment widely used for parts subject to fatigue and wear in application. Surface hardening is obtained through the carbon enrichment of the surface layers up to the eutectoidic composition and the heat treatment, which form a stress relieved martensitic case. Due to the high carbon content, the surface microhardness is usually greater than that of through hardened steels. In some conditions, the benefits deriving from the surface hardening may be eliminated by the embrittlement. In this work, the results of lubricated rolling-sliding tests of a carburized 1.5% Mo steel are presented, discussing the conditions that may cause brittle cracking of the surface. A theoretical analysis is also proposed, and introduced in a design methodology to select the material characteristics for the lubricated rolling-sliding and rolling-sliding wear.

EXPERIMENTAL PROCEDURE

The powder used for the production of the specimens is the 1.5% Mo prealloyed iron, to which 0.3% graphite was added. Rings with 16 mm internal diameter, 40 mm external diameter and 10 mm height were cold compacted and sintered at 1150°C in endogas. The sintered density is 7.3 g/cm^3. Gas carburizing in endogas and stress relief at 180°C in air were carried out.

Lubricated rolling-sliding tests were carried out on an Amsler tribometer, using the Castrol edge 5W-30 oil as lubricant. The counterface rings were made of the 1%C and 1.5%Cr bearing steel hardened at 62 HRc. 10% sliding was obtained by setting the rotation speed of the specimen and the counterface at 400 rpm and 360 rpm, respectively. The friction coefficient was continuously recorded during the tests. Tests were run up to one million of cycles and the formation of cracks was investigated by the metallographic analysis of the worn specimens.

RESULTS AND DISCUSSION

Figure 2 shows the microstructure of the case and of the bulk of the carburized steel. The surface microstructure is martensitic, with some retained austenite, while the core is bainitic.

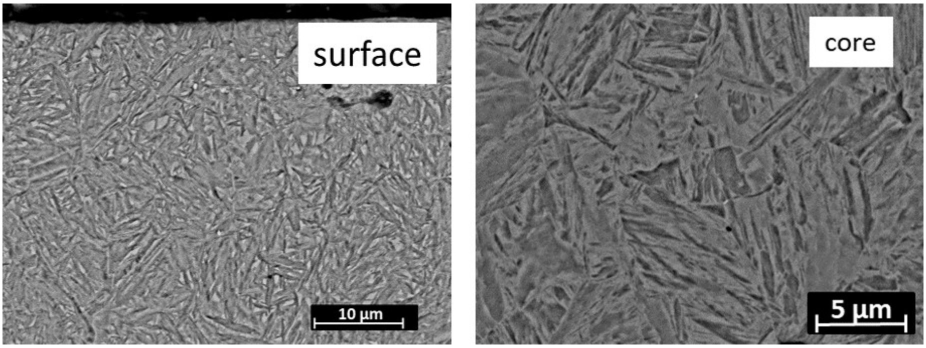

Fig.2. Microstructure of the carburized steel.

Figure 3 shows the microhardness profile of the carburized steel (left) and the results of the theoretical prediction of the resistance to the formation of subsurface cracks.

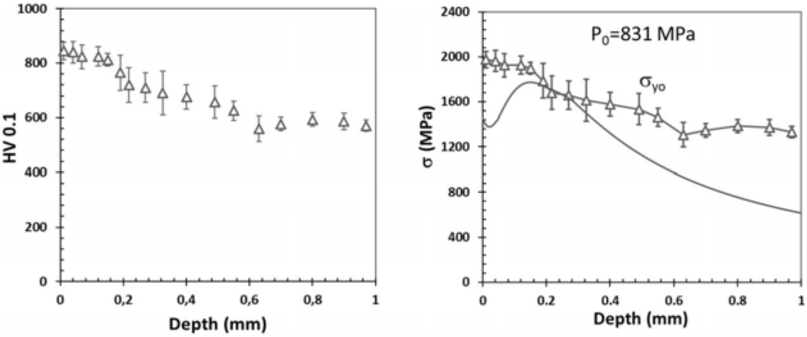

Fig.3. Microhardness profile of the carburized steel (left) and comparison between yield strength of the matrix and equivalent stress corresponding to 831 MPa mean Hertzian pressure.

From the microhardness profile (left plot) the profile of the yield strength of the matrix was calculated (line connecting the triangles in the right plot), and the maximum stress profile tangent to the yield strength one was determined (continuous line). The corresponding mean Hertzian pressure is 831 MPa. To verify the theoretical prediction, lubricated rolling-sliding tests were carried out at two mean pressures: 800 MPa and 850 MPa [9]. The metallographic analysis of the worn specimens shown subsurface cracks in the specimen tested at the higher mean pressure and no cracks in the other one, confirming the theoretical prediction. However, some cracks were observed in the surface layers of the latter, as those shown in Fig.4.

In particular the crack on the left side, perpendicular to the surface, can be attributed to a brittle damage caused by the tensile surface stress.

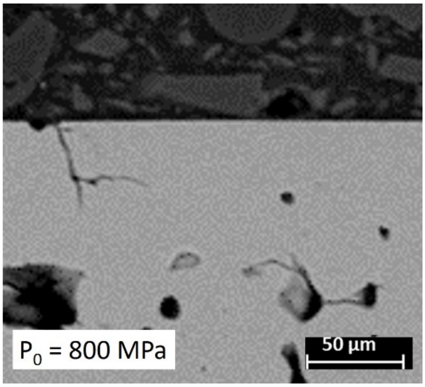

Fig.4. Example of brittle cracks in the surface layers of the worn carburized specimen.

The formation of a surface brittle crack occurs when the surface tensile stress σ_t exceeds the resistance of the material to the brittle fracture σ_f.

With reference to figure 5, the surface tensile stress is the tangential one along direction x. It is strongly dependent on the friction coefficient, as shown in the figure right, where the normalized tangential stress is plotted for three different values of μ.

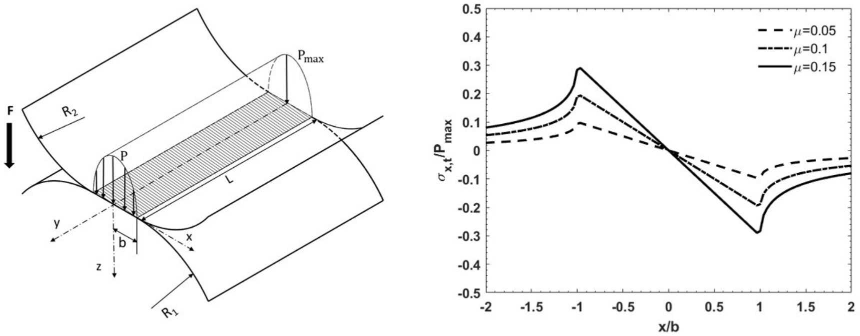

Fig. 5. Schematic representation of the contact pressure and effect of the friction coefficient on the normalized tangential stress.

The maximum tensile stress σ_t can be determined through equation (3)

$$\sigma_t = \frac{2P_{\max}\beta_k\mu}{M_{r2}} \tag{3}$$

where P_{max} is the maximum Hertzian pressure, μ is the friction coefficient and M_{r2} is the load bearing surface determined from the Abbott-Firestone diagram [10]. It is 0.85 for the carburized disks of the present investigation. The dependence of the tensile stress on M_{r2} and on the friction coefficient for different values of the mean Hertzian pressure P_0 (= 0.78 P_{max}) is shown in Fig.6.

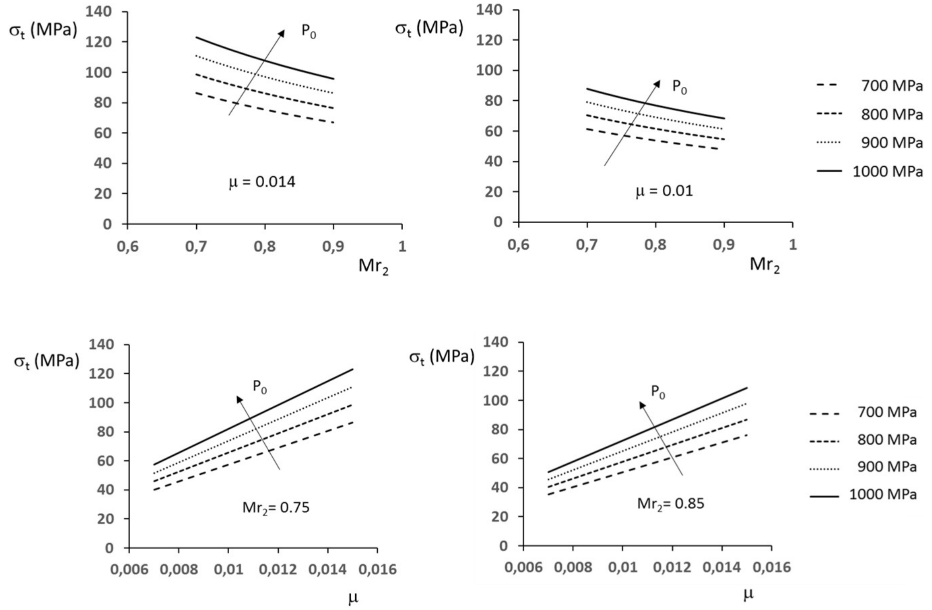

Fig.6. Surface tensile stress as a function of the load bearing surface (upper) and of the friction coefficient (lower) for different values of the mean Hertzian pressure.

The load bearing surface and the friction coefficient were varied within reasonable ranges in practical applications. The figure shows that friction coefficient has a great effect: even small variations may lead to a significant increase of the tensile stress.

The fracture stress is given by equation (4)

$$\sigma_f = \frac{K_{IC}}{\psi\sqrt{\pi\alpha}} \tag{4}$$

where K_{IC} is the fracture toughness of the matrix, Ψ is a geometrical parameter and *a* is the defect size. The fracture toughness may be determined by the yield strength of the matrix through eq. (5) [8]

$$K_{IC} = \frac{6000}{\sigma_{yo} + 300} \tag{5}$$

The defect size is the dimension of the larger pore on the surface. It may be measured by Image Analysis, that returns different parameters relevant to the pore size. Figure 7 shows two examples of the large pores observed on the specimen surface: the original image, the digitalized one and two parameters, the equivalent diameter D_{eq} and the maximum Feret diameter D_{max}.

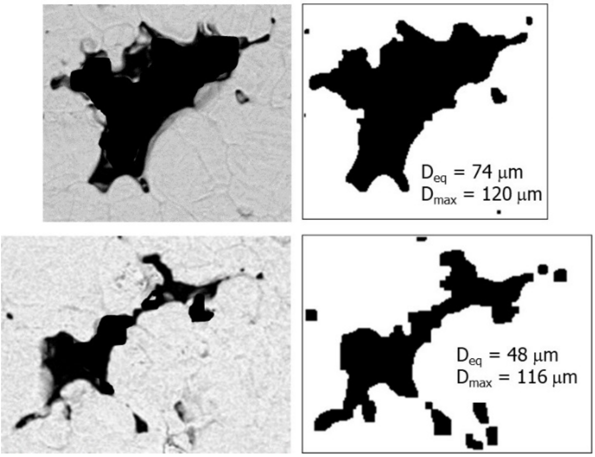

Fig.7. Examples of the large surface pores with equivalent diameter D_{eq} and maximum Feret diameter D_{max}.

The equivalent diameter is the diameter of the circle having the same area of the pore. It underestimates the effect of the pore on the crack propagation when pores are elongated as those in the figure. Therefore, the half of the maximum Feret diameter was taken as representative of the defect size in eq. (4).

Figure 8 shows the effect of the defect (pore) size and microhardness on σ_f.

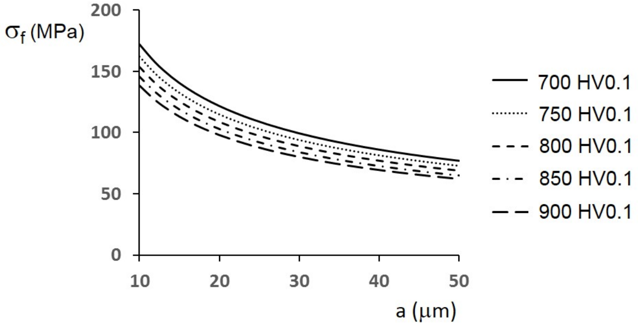

Fig.8. Effect of the defect (pore) size and microhardness on σ_f.

The resistance of the material to the propagation of the brittle fracture decreases with microhardness, due to the decrease of the fracture toughness, and with the pore size.

By combining equations (3) and (5) an expression for the critical pore size may be obtained, as by eq. (6).

$$\alpha = \frac{1}{4\psi^2\pi} K_{IC}^2 \left(\frac{M_{r2}}{\beta_k}\right)^2 \left(\frac{1}{\mu P_{\max}}\right)^2 \qquad (6)$$

It represents the minimum pore size that causes brittle cracking on the surface under the tensile stress.

Figure 9 shows the effect of the mean pressure and the friction coefficient on the critical pore size for a constant load bearing surface and two different microhardness values.

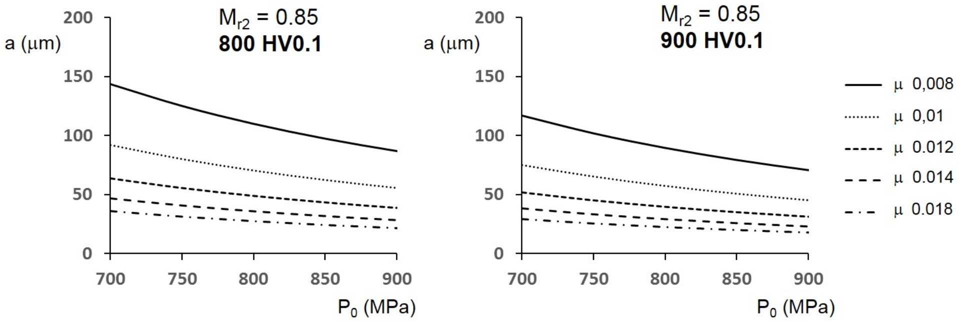

Fig.9. Effect of the mean pressure and the friction coefficient on the critical pore size.

This kind of diagram may be used to discuss the experimental evidence above described. Considering that:

- the maximum Feret diameter of the surface pores is 120 μm, that results in a defect size of 60 μm;
- the friction coefficient recorded during the tests at 800 MPa and 850 MPa mean pressure is 0.014;
- the surface microhardness of the carburized steel is 830 HV0.1;

Figure 10 shows that at 831 MPa mean pressure (the theoretical resistance to the formation of subsurface fatigue cracks) the formation of brittle cracks is predicted by the theoretical model.

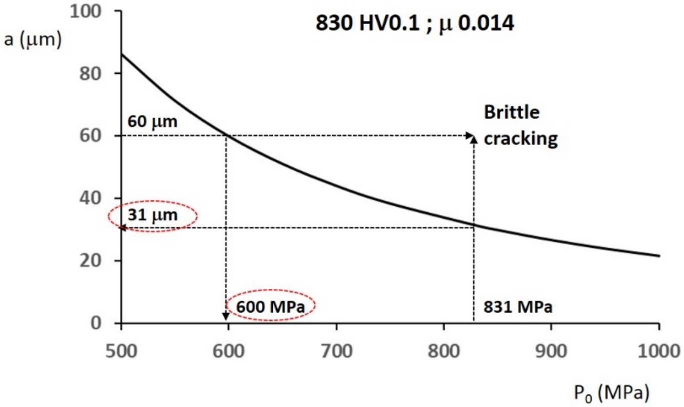

Fig.10. Theoretical prediction of the occurrence of brittle surface cracks in the carburized ring: effect of the pore size and the mean Hertzian pressure.

The brittle cracks are also expected at 800 MPa mean pressure, as observed experimentally. The figure also indicates that a maximum defect size of 31 μm, corresponding to a maximum Feret diameter of 62 μm, should prevent the formation of brittle cracks at 831 MPa. Such a maximum pore size could be obtained either strongly reducing the particle size or further increasing density, but both solutions are not practicable. The two real options are therefore surface densification and shot peening; the former reduces pore size dramatically, the latter introduces surface compressive residual stresses [9]. The material with the combination of the measured maximum Feret diameter and microhardness shown above would resist to the surface brittle cracking at a mean pressure of 600 MPa.

The resistance to brittle fracture may be increased through the fracture toughness by reducing microhardness. Figure 11 shows that microhardness should be decreased down to 560 HV0.1 to prevent brittle damage, but the resistance to the subsurface plastic deformation and fatigue crack nucleation would be seriously impaired.

Finally, the effect of the efficiency of lubrication is shown in Fig.12.

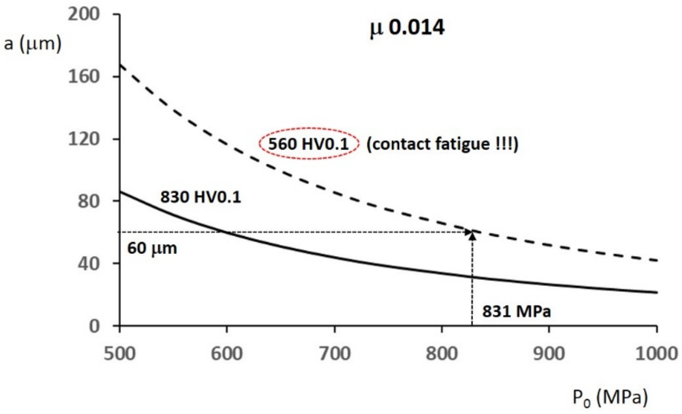

Fig.11. Theoretical prediction of the occurrence of brittle surface cracks in the carburized ring: effect of the surface microhardness.

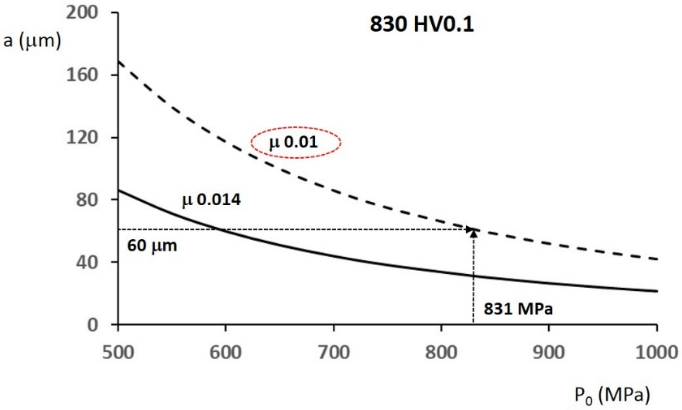

Fig.12. Theoretical prediction of the occurrence of brittle surface cracks in the carburized ring: effect of the friction coefficient.

The carburized steel with the measured maximum Feret diameter and microhardness shown above is expected to survive to brittle surface cracking if the friction coefficient is kept below 0.01. This indication confirms the great effect of the friction coefficient, and the importance to control the efficiency of lubrication.

All the theoretical work here presented may be implemented in the design procedure shown in Fig. 13.

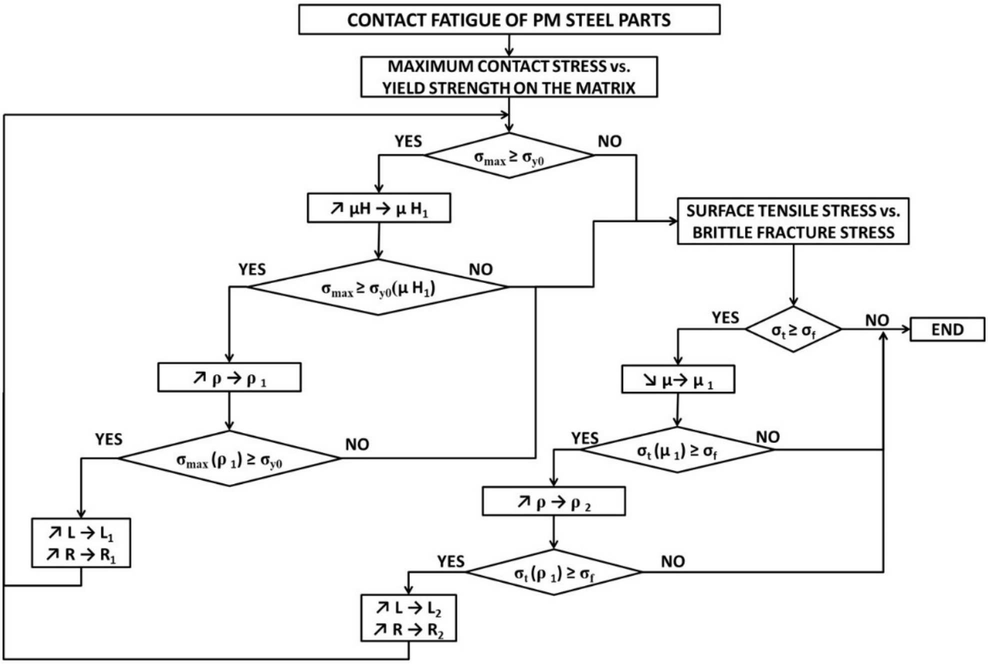

Fig.13. Design procedure for lubricated rolling and rolling-sliding.

The procedure starts checking the occurrence of the subsurface plastic deformation. If the maximum stress is greater than the yield strength of the matrix, a subsurface crack is expected to nucleate. Three possible solutions are sequentially verified:

- the increase in microhardness to increase the yield strength of the matrix;
- the increase in density to decrease the maximum contact stress;
- the change of the geometry of the parts, either increasing the contact radii or the contact length.

If the yield strength of the matrix results greater than the maximum contact stress either at the first verification or after the implementation of the three possible solutions, the nucleation of subsurface fatigue cracks will be prevented. The verification of the surface brittle cracking is then carried out.

If the tensile stress is greater than the resistance to brittle fracture of the material, the possible solutions are, in sequence:

- the control of the lubrication conditions, to reduce the friction coefficient;
- the increase in density to reduce the maximum pore size;
- the change of the geometry of the sintered part, to reduce the mean Hertzian pressure.

If the resistance to brittle fracture of the material results greater than the tensile stress either at the first verification or after the implementation of the three possible solutions, surface brittle cracking will be prevented.

CONCLUSION

The lubricated rolling-sliding behavior of a 7.3 g/cm^3 carburized 1.5%Mo - 0.25%C sintered steel was studied to verify the possible formation of surface brittle cracks due to the combined effect of the high surface microhardness and large surface pores. The resistance to the subsurface fatigue crack nucleation (contact fatigue) was determined in a previous work, resulting in a mean Hertzian pressure of 831 MPa. Tests at 800 MPa did not cause any subsurface cracking, but some surface cracks were observed in the worn specimens, attributable to a brittle behavior. Such a damage limits/eliminates the effect of carburizing on the resistance of the steel to contact fatigue.

The phenomenon was analyzed theoretically comparing the surface tensile stress to the fracture stress of the material. The resistance of the carburized steel to surface brittle cracking increases by increasing the load bearing surface and by decreasing the maximum pore size, the surface microhardness and the friction coefficient. In particular this last parameter plays a crucial role, since it greatly affects the surface tensile stress. Indeed, the decrease of the friction coefficient from 0.014 down to 0.01 increases the resistance to surface brittle cracking of the investigated material from 600 MPa to 831 MPa mean Hertzian pressure.

The theoretical analysis was implemented in a design procedure for parts subject to contact stresses, aiming at selecting the material and its heat treatment for a specific application, where contact stresses may cause both contact fatigue and brittle surface cracking.

REFERENCES

[1] Metinoz, I., Cristofolini, I., Pahl, W., Molinari, A.: Materials Science and Engineering A, vol. 614, 2014, p. 81
[2] Molinari, A., Metinoz, I., Cristofolini, I.: Powder Metallurgy Progress, vol. 14, 2014, n.1, p. 32
[3] Donzella, G., Petrogalli, C.: International Journal of Fatigue, vol. 32, 2010, p. 256
[4] Bell, T., Sun, Y.: Surface Engineering, vol. 6, 1990, p.133
[5] Tesfaye, S., Molinari, A., Pahl, W.: Powder Metallurgy, vol. 60, 2017, p. 231
[6] Pohl, D.: Powder Metallurgy International, vol. 1, 1969, p. 26
[7] Molinari, A., Menapace, C., Santuliana, E.: Powder Metallurgy Progress, vol. 11, 2011, p. 12
[8] Straffelini, G., Menapace, C., Molinari, A.: Powder Metallurgy, vol. 45, 2002, n. 2, p. 167
[9] Tesfaye, S., Molinari, A., Pahl, W., Denicolo, A., Marconi, P.: Advances in Powder Metallurgy & Particulate Materials, vol. 6, 2017, p. 589
[10] Cristofolini, I., Cipolloni, G., Molinari, A.: Advances in powder Metallurgy and Particulate Materials, vol. 2, 2012, p. 47

Powder Metallurgy Progress, Vol.18 (2018), No.1, p.031-039
http://dx.doi.org/10.1515/pmp-2018-0004

MANUFACTURING OF VALVE BRIDGE COMPONENT UTILIZING LEAN ALLOYED POWDERS AND VACUUM SINTERING

R. Shvab, M. V. Sundaram, H. Karlsson, D. Chasoglou, S. Berg, E. Hryha, L. Nyborg

Abstract
Increasing the application area of powder metallurgy (PM) steels for manufacturing of high-performance structural components results in material saving, reduction in energy consumption, etc. In this study, feasibility of the manufacturing of valve bridge component for heavy duty engine utilizing lean alloyed powders and novel vacuum sintering approach, followed by low pressure carburizing, is studied. Three low alloyed steel powders were processed by conventional uniaxial pressing and sintering at 1120 and 1250°C in industrial vacuum furnace. The components were tested under high cycle fatigue testing, simulating real conditions of operation. Fatigue properties did not show significant dependence on the sintering temperature and were comparable to currently used reference cast material. Fracture surfaces of broken samples were analyzed to detect crack initiations and fracture mechanisms as well as quality of sintering. Results showed preferentially ductile failure, well developed sintering necks and clean pore surfaces, indicating good sintering. Tested material in combination with novel vacuum sintering process show to be an attractive alternative for manufacturing of this type of components for heavy duty engine applications.

Keywords: Powder metallurgy, low alloyed steel, high cycle fatigue, fracture, sintering, low pressure carburizing.

INTRODUCTION

Powder metallurgy is referred to be a cost efficient and sustainable manufacturing processes for near-net-shaped production [1]. It covers huge variety of applications – from structural components to biomedical applications [2-5]. PM steels have become the most significant products of PM technology today and account for more than 80% of the total volume of all materials produced. Improvement in the quality of powder, development of new alloy systems and sophistication in the processing techniques have extended the range of applications for sintered ferrous and ferrous alloy parts [6]. Due to the high surface area present for the case of PM steel powders, they are subject to significant risk of oxidation. For this reason, traditionally, alloying elements such as Cu, Mo and Ni have been used as they are easily reducible during conventional sintering process.

Ruslan Shvab, Maheswaran Vattur Sundaram, Eduard Hryha, Lars Nyborg: Department of Industrial and Materials Science, Chalmers University of Technology, Rännvagen 2A, 412 96 Göteborg, Sweden
Henrik Karlsson: Volvo Group Trucks Technology, Göteborg, Sweden
Dimitris Chasoglou, Sigurd Berg: Höganäs AB, Höganäs, Sweden

However, utilizing Cr as an alloying element becomes more interesting nowadays. One of the main advantages is the economic benefit since Cu and Ni are significantly more expensive than Cr. Furthermore, Cr has higher hardenability which makes it suitable for high performance applications and sinter-hardening [7]. The major challenge concerning usage of Cr as an alloying element is its high oxygen affinity, which put strict demands on processing. By prealloying, the activity of chromium can be reduced and for the low levels of chromium, prealloying does not significantly degrade compressibility of the powders [8]. Taking into account the advantages of low Cr alloyed PM steels, they become more and more interesting for high performance applications. On the other hand, the mechanical properties depend very much on the microstructure, density and pores characteristics [9-12]. It gives some freedom and possibility to tune the PM material properties in the required way. Usage of different heat treatment processes including low pressure carburization (LPC) and gas quenching [13], as a separate process or integrated in modern vacuum furnaces, is another advantage of using PM manufacturing process.

MATERIALS AND METHODS

Two commercial alloys, namely Astaloy CrA and Distaloy DH, and experimental low Cr alloyed powder were used as based materials in this investigation. All powders were supplied by Höganäs AB, Sweden. Powders were admixed with natural graphite (UF4, Kropfmühl) and lubricant (Lube E). Composition of the respective mixes is summarized in Table 1.

Table 1. Composition of powder mixes.

Base powder	Cu, wt.%	Ni, wt.%	C, wt.%	Lube E, wt.%
Low Cr alloyed	2	-	0.65	0.6
Astaloy CrA (Fe-1.8Cr)	-	1	0.45	0.6
Distaloy DH (Fe-2Cu-1.5Mo)	-	-	0.6	0.6

Abovementioned powder mixes were pressed into cylindrical blocks, vacuum sintered and machined to receive a valve bridge component shape, see Figure 1.

Fig.1. „Side“ (up) and „bottom“ (down) view of the valve bridge component prototype for heavy duty engine application.

Vacuum sintering followed by the low pressure carburizing was done in a two chamber furnace with high pressure gas quench, Fulgura Duo by ECM Technologies. Sintering was performed at both 1120 and 1250°C for 30 min for all the investigated materials. Acetylene diluted with nitrogen was used as carburizing gas and the samples were quenched with nitrogen under 20 bars pressure.

The high cycle fatigue properties of the valve bridges were tested in the RUMUL vibrophore machine. Loads were measured with the built in load cell. The fixture consisted of two valve shafts cut and fitted into a 25 mm thick steel plate. The diameter of the valve shafts were 10 mm. A flat wedge with a rounded top was used for load application in the middle between the valve shafts to create a 3 point bending load, see Figure 2. Fatigue testing frequency was 112 Hz. The cycling was carried out until the frequency dropped 3 Hz.

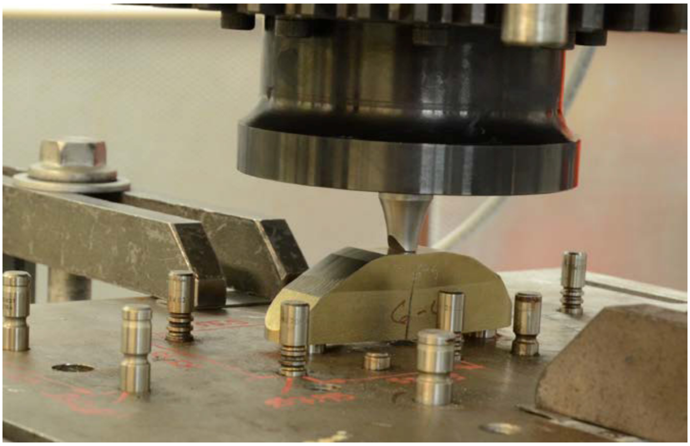

Fig.2. High cycle fatigue testing set-up.

Materials after testing were analysed by light optical microscopy (Leitz DMRX) to obtain representative microstructures. Fracture surfaces of broken samples were analysed by stereo microscope SteREO Discovery.V20 and scanning electron microscope LEO Gemini 1550 (LEO GmbH, Oberkochen, Germany) in order to detect crack initiations, quality of sintering and fracture mechanisms.

RESULTS AND DISCUSSION

High cycle fatigue testing

High cycle fatigue tests were performed at Volvo Group Trucks Technology, Göteborg, Sweden, to simulate the real operating conditions for investigated materials. Preliminary tests showed preferential fracture of the samples in the hole, due to a sharp corner inside the hole induced by machining. To avoid such failure, grinding and radii shot peening was applied. Further tests showed fracturing in the middle part of the sample, see Figure 2. Results presented in Figure 3 give the overview of the fatigue behaviour of new investigated materials prepared by powder metallurgy route in comparison to currently used cast material. Results showed that low pressure carburised Astaloy CrA material has strength similar to the reference material. Moreover, Astaloy CrA samples did not break even after 10^7 cycles. At the same time, low Cr alloyed material and Distaloy DH showed lower fatigue strength than reference material. No significant influence of sintering temperature on the fatigue strength of materials was revealed by fatigue tests. Surface hardness measured in the area of loading application showed slightly higher values for materials sintered at 1250ºC in comparison to ones sintered at 1120ºC, see Table 2. Surface hardness of Astaloy CrA and low Cr alloyed materials are comparable to each other, while Distaloy DH has slightly lower values.

Taking to account that prototypes of valve bridge components tested in this study were machined from cylindrical blocks – their geometry, shape and size of the holes, surface hardness and density are not optimized. Further improvement of abovementioned parameters will increase fatigue strength of investigated materials.

Tab. 2. Surface hardness of investigated materials.

Material	Sintering temperature, ºC	Surface hardness, HV10
Low Cr alloyed	1120	477±7
Low Cr alloyed	1250	506±28
Astaloy CrA	1120	467±20
Astaloy CrA	1250	505±32
Distaloy DH	1120	438±17
Distaloy DH	1250	482±15

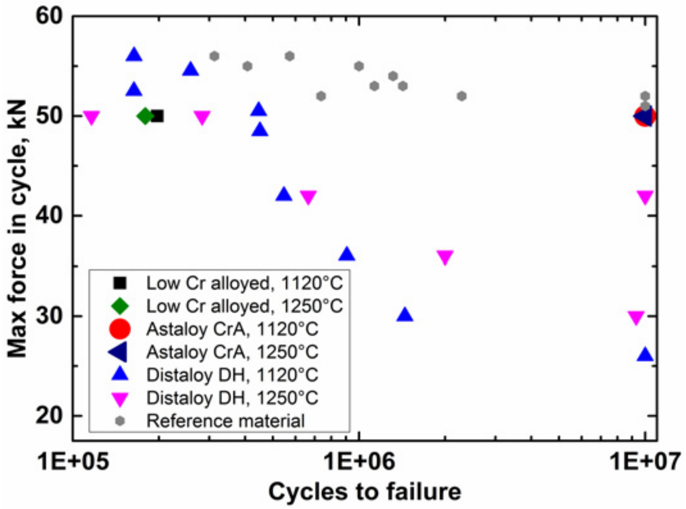

Fig.3. Fatigue tests results for investigated materials in comparison to the reference material.

Metallographic investigation

The example of pores structure of investigated materials sintered at 1120ºC presented in the Figure 4. In all cases pores are well distributed in the material. Low Cr alloyed material contains large pores, most probably due to admixed Cu powder.

The microstructure of low Cr alloyed material is mostly martensitic with areas of ferrite and pearlite, see Figure 5.

The microstructure of Astaloy CrA material contains martensite with Ni-rich austenite areas and some bainite, see Figure 6. Areas of austenite and bainite are smaller for material sintered at 1250ºC due to better diffusion at higher temperature.

In the case of Distaloy DH, the microstructure was martensitic, see Figure 7.

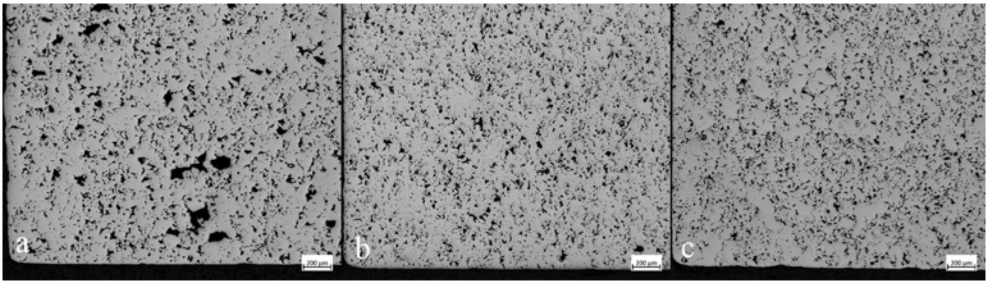

Fig.4. None-etched microstructure of low Cr alloyed steel (a), Astaloy CrA (b) and Distaloy DH (c) materials sintered at 1120ºC.

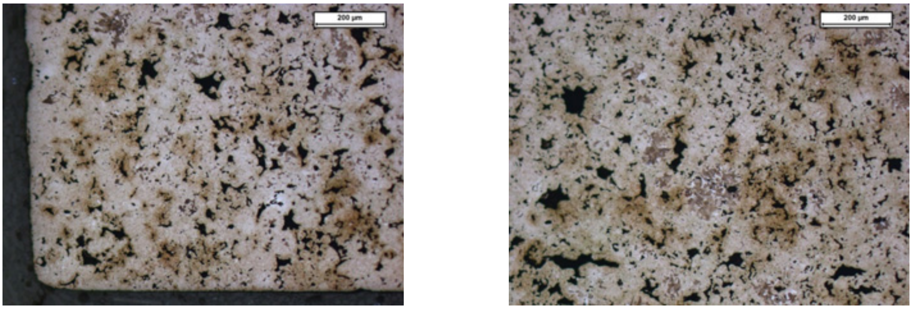

Fig.5. The microstructure of low Cr alloyed material sintered at 1120ºC.

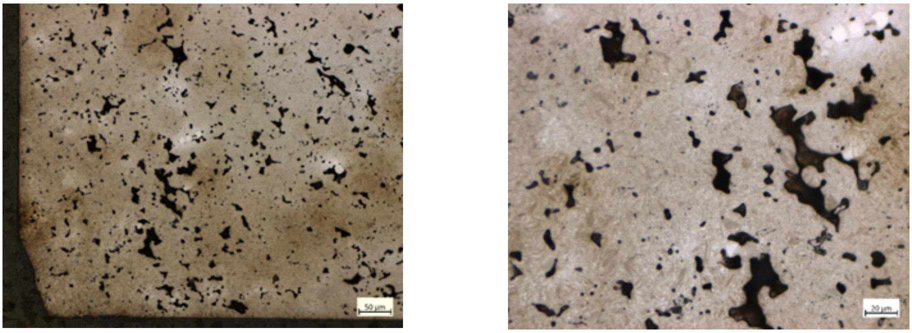

Fig.6. The microstructure of Astaloy CrA material sintered at 1120ºC.

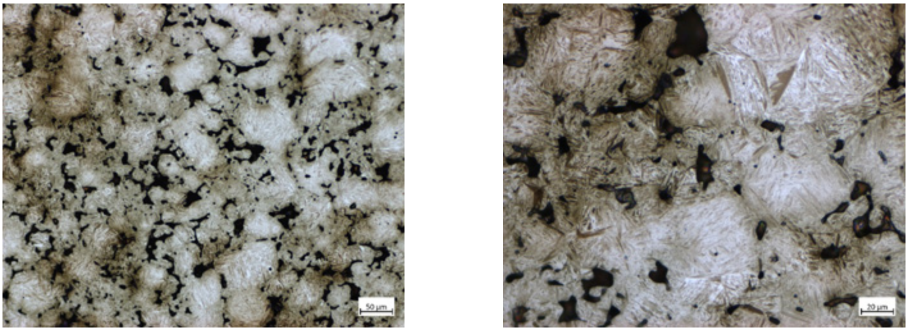

Fig.7. The microstructure of Distaloy DH material sintered at 1120ºC.

Fracture surface analysis

In order to find the crack initiation sites, identify the fracture mechanisms and check the quality of the sintering, the fracture surface analysis was performed for the broken samples. In the case of low Cr alloyed powder sintered at both 1120 and 1250ºC, crack initiations were detected close to the sample surface. For material sintered at 1120ºC the initiation site was found at the „bottom“ of the sample, see Figure 8a, while for 1250ºC sintered material it was closer to the „side“ of the sample, see Figure 8b.

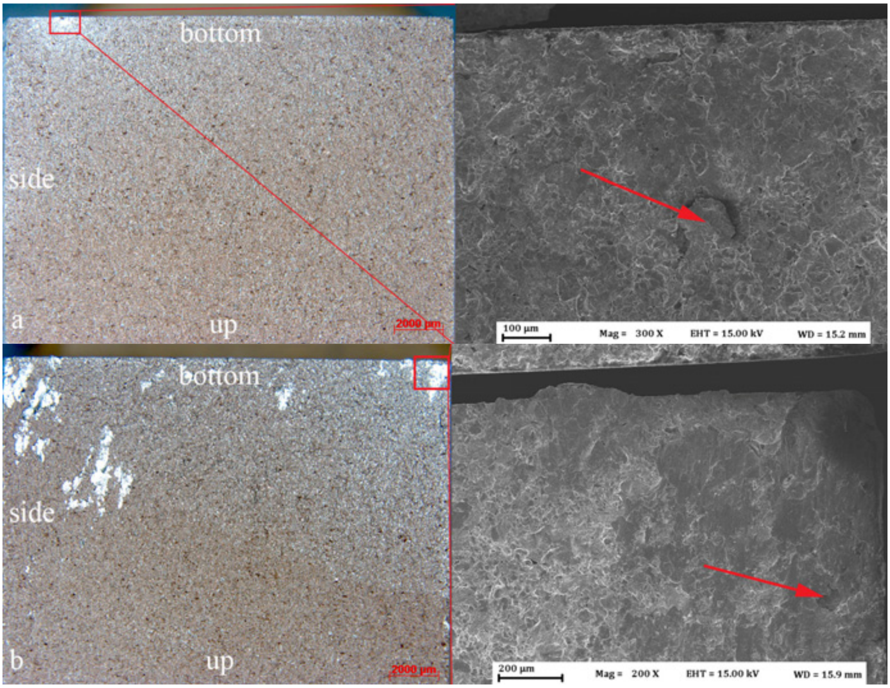

Fig.8. Crack initiations for low Cr alloyed material samples sintered at a) 1120, b) 1250ºC.

Inter and transparticle ductile fracture was found to be the main failure mechanism for low Cr alloyed material sintered at both 1120 and 1250ºC temperatures, see Figure 9. Some areas with cleavage were also observed. No siginifacant oxide residues were detected, indicating good sintering.

For the valve bridges made of Distaloy DH powder material and sintered at both 1120 and 1250ºC, crack initiation sites were found at the bottom edges of the component, see Figure 10.

Similarly to low Cr alloyed material, ductile fracure was the main mechanism of failure for Distaloy DH material sintered at both 1120 and 1250ºC temperatures, see Figure 11. Well developped sintering necks with absence of residual oxides indicate good quality of sintering process.

Since valve bridge components made of Astaloy CrA material did not brake during high cycle fatigue testing, there was no fracture surface available for the investigation.

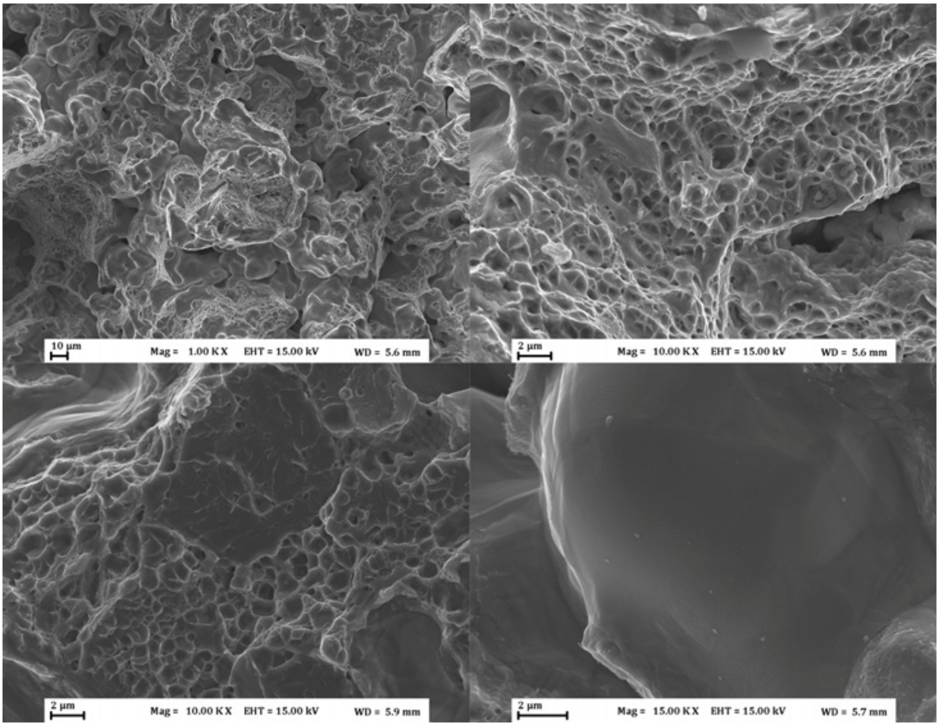

Fig.9. Fracture surface of low Cr alloyed material sintered at 1120ºC.

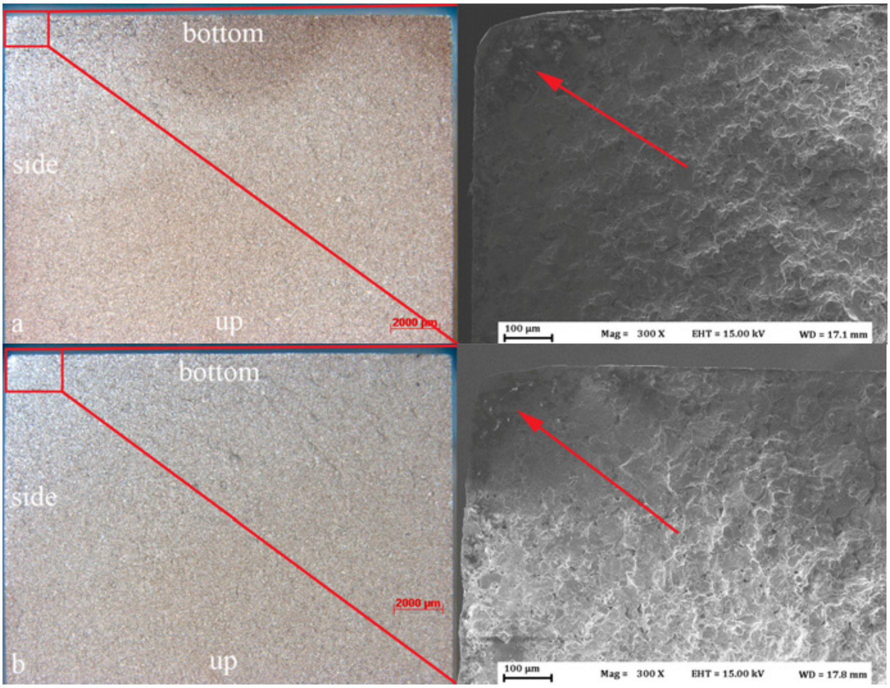

Fig.10. Crack initiations for Distaloy DH powder samples sintered at a) 1120, b) 1250ºC.

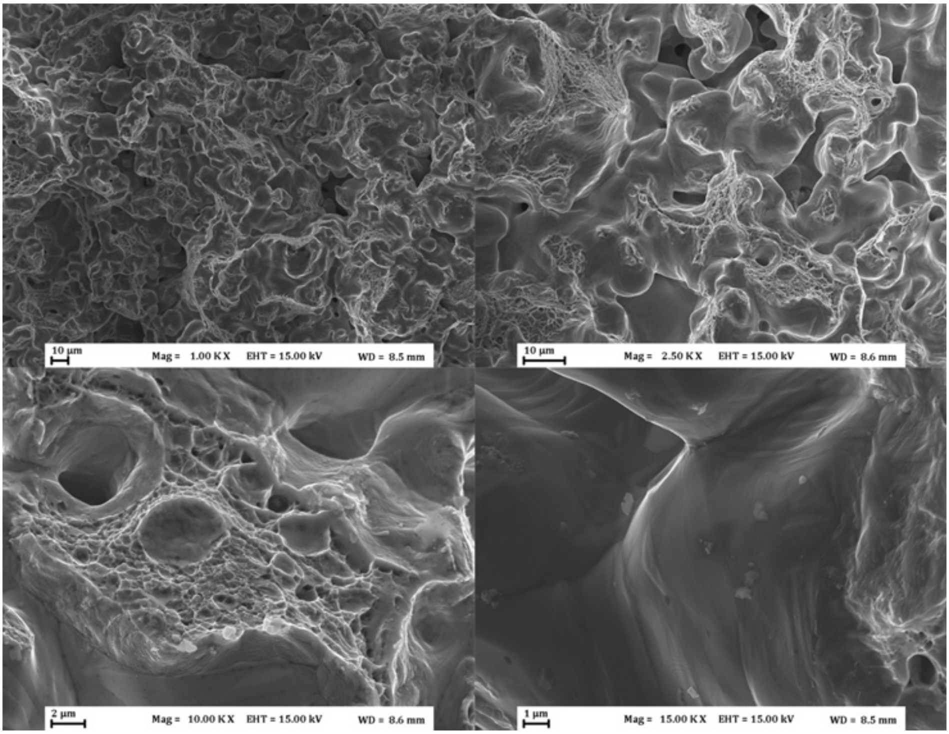

Fig.11. Fracture surface of Distaloy DH material sintered at 1120ºC.

CONCLUSION

The possibility of manufacturing of valve bridge component for heavy duty engine application utilizing lean prealloyed with Cr steel powder in combination with novel vacuum sintering and low pressure carburising was confirmed as an attractive alternative. Astaloy CrA material showed the same and even better performance in high cycle fatigue test as currently used cast material, and did not break even after 10^7 cycles. Sintering temperature showed no sinificant influence on the fatigue properties. Two other investigated materials – experimental low Cr alloyed PM steel and Distaloy DH – revealed lower fatigue strength compared to the reference material. Fracture surface analysis showed preferentially ductile failure, well developed sintering necks and absence of oxides residue, indicating good sintering in vaccum. Metallographic investigation showed mostly martensitic microstructure for all the materials. Presence of large pores was observed for low Cr alloyed and Distaloy DH materials, which can explain lower fatigue strength ot these materials.

Acknowledgement

Funding from the Swedish Agency for Innovation Systems (VINNOVA) in the frame of the project No: 2014-00795 is greatly acknowledged. Support from the Chalmers Areas of Advance in Production as well as funding from the strategic innovation program LIGHTer, provided by Vinnova, are gratefully acknowledged.

REFERENCES

[1] Karamchedu S., Hryha E., Nyborg L.: J. Mater. Process. Technol., vol. 223, 2015, p.171.

[2] Danninger H., Xu C., Khatibi G., Weiss B, Lindqvist B.: Powder Metall., vol. 55, 2013, p. 378.

[3] Bidulsky R., Actis Grande M., Dudrova E., Kabatova M., Bidulska J., Powder Metall., vol. 59, 2016, p. 121.

[4] Danninger H., Sohar C., Gierl C., Betzwar-Kotas A., Weiss B.: Mater. Sci. Forum, vol. 672, 2011, p. 23.

[5] Kupkova M. et al.: Arch. Metall. Mater., vol. 60, 2015, p. 639.

[6] Karamchedu S.: “Critical Aspects of Delubrication and Sintering of Chromium-alloyed Powder Metallurgy Steels”, PhD Thesis, Chalmers University of Technology, Gothenburg, Sweden, 2015.

[7] Berg S.: Adv. Powder. Metall. Part. Mater., vol. 5, 2001, p. 5.

[8] Hryha E., Dudrova E., Bengtsson S.: Powder Metall., vol. 5, 2007, p. 3.

[9] Delarbre P., Schoppa A., Hornof B.: Met. Powder Rep., vol. 71, 2016, p. 344.

[10] Torralba J. M., Esteban L., Bernardo E., Campos M.: Powder Metall., vol. 57, 2014, p. 357.

[11] Mousavinasab S., Blais C.: Mater. Sci. Eng. A, vol. 667, 2016, p. 444.

[12] Azadbeh M., Mohammadzadeh A., Danninger H., Gierl-Mayer C.: Metall. Mater. Trans. B, vol. 46B, 2015, p. 1471.

[13] Dahlström M.: Advances in Powder Metallurgy and Particulate Materials - 2014, Proceedings of the 2014 World Congress on Powder Metallurgy and Particulate Materials, PM 2014, p. 660.

Powder Metallurgy Progress, Vol.18 (2018), No.1, p.040-048
http://dx.doi.org/10.1515/pmp-2018-0005

EFFECT OF POWDER RECYCLING ON THE FRACTURE BEHAVIOR OF ELECTRON BEAM MELTED ALLOY 718

H. Gruber, P. Karimi, E. Hryha, L. Nyborg

Abstract
Understanding the effect of powder feedstock alterations during multi-cycle additive manufacturing on the quality of built components is crucial to meet the requirements on critical parts for aerospace engine applications. In this study, powder recycling of Alloy 718 during electron beam melting was studied to understand its influence on fracture behavior of Charpy impact test bars. High resolution scanning electron microscopy was employed for fracture surface analysis on test bars produced from virgin and recycled powder. For all investigated samples, an intergranular type of fracture, initiated by non-metallic phases and bonding defects, was typically observed in the regions close to or within the contour zone. The fracture mode in the bulk of the samples was mainly moderately ductile dimple fracture. The results show a clear correlation between powder degradation during multi-cycle powder re-use and the amount of damage relevant defects observed on the fracture surfaces. In particular, samples produced from recycled powder show a significant amount of aluminum-rich oxide defects, originating from aluminum-rich oxide particulates on the surface of the recycled powder.

Keywords: additive manufacturing of Alloy 718, electron beam melting, powder recycling, powder degradation, fractography of AM components

INTRODUCTION

Powder bed fusion additive manufacturing (AM) is a rapidly growing manufacturing method that has attracted increasing attention in both industry and academia during the last years. A key advantage of this process is the inherent ability of near-net shape production of structurally optimized, complex geometry components together with the potential to reduce material consumption. One such method is electron beam melting (EBM) in which the component is built by fusing together thin layers of metal powder using a focused electron beam.

Alloy 718 (commonly referred to as Inconel 718 or IN718 - Inconel 718 is a trade mark of the Special Metals Corporation group of companies) is an age-hardenable nickel-iron base superalloy that offers an excellent combination of good mechanical properties, oxidation and corrosion resistance up to around 650°C. It is one of the most widely used superalloys and is predominantly found in aeronautic engine components such as turbine and compressor discs, turbine shafts and compressor blades [1-3].

Hans Gruber, Eduard Hryha, Lars Nyborg: Department of Industrial and Materials Science, Division of Materials and Manufacture, Chalmers University of Technology, Gothenburg, SE-412 96, Sweden
Paria Karimi: Department of Engineering Science, Additive Manufacturing Group, University West, SE-46186 Trollhättan, Sweden

The production route of aerospace components has traditionally involved extensive machining often resulting in low buy-to-fly ratios. Also, the high room-temperature hardness of such alloys results in high tool wear and poor workpiece surface integrity when applying conventional, subtractive manufacturing methods. Therefore, due to its ease-of-fabrication capabilities and potential material cost savings, AM has been recognized by the aerospace industry as an attractive alternative production method [4-5]. However, components for such applications are exposed to an adverse set of mechanical, thermal and chemical loads resulting in strict quality control throughout the whole manufacturing chain from raw material to final product [6].

Even though additive manufacturing is capable of producing parts of equal or even superior mechanical performance compared to casting or forging, there is still a need for greater understanding regarding process stability and defect formation to ensure high resistance to, for example, crack initiation during cyclic loading [7].

Due to the relatively high cost of the metal powder feedstock used for AM, the permitted number of powder re-use times before risking a loss in the part performance has a significant influence on its cost-effectiveness. Studies have been performed to understand the importance of different physical and chemical powder characteristics on the process robustness and quality of fabricated parts and attempts have been made to assess the stability of the powder feedstock for use over extended time periods [5]. However, more knowledge is required to understand the effect of powder degradation on the final properties of the built components.

This work was done to study the fracture characteristics of EBM processed Alloy 718. Fracture surface analysis was performed to understand the effect of powder degradation on defect formation and fracture behavior of test samples produced from virgin and multi-cycle re-used powder.

MATERIALS AND METHODS

In the present study, EBM was used to fabricate standard Charpy V-notch (CVN) impact test bars from pre-alloyed Alloy 718 powder using an Arcam A2X EBM system located at University West, Trollhättan, Sweden. The powder feedstock material was commercial plasma-atomized powder provided by Arcam AB, Sweden. It had a powder size distribution of 45-105 μm and a chemical composition resembling the nominal composition of Alloy 718 as presented in Table 1.

Tab.1. Chemical composition of the Alloy 718 powder.

Element	Ni	Cr	Fe	Nb	Mo	Ti	Al	Mn	C	Co	Ta	B	Si	P	S
wt.%	54.1	19.0	16.9	5.0	3.0	1.0	0.5	0.1	0.3	0.04	<0.01	0.001	0.06	0.004	<0.001

The EBM process operates in a helium atmosphere at a partial vacuum level of 2×10^{-3} mbar. During the whole process the complete powder bed is held at an elevated temperature (around 1000°C for Alloy 718). The part is built by alternating raking, sintering and melting of thin layers of metal particles. For each layer, a contour exposure is applied for consolidation along the component edges followed by a hatching exposure at the core. It should be noted that the differences in scanning strategies between contour and hatch region result in very different microstructures at the sample edges as compared to the bulk region [8]. After completion, the components are left to cool to a temperature below 100˚C before they are removed from the process chamber. A more detailed description of the EBM process can be found in for example V. Sames et al. [9] or in H. Gruber et al. [10].

In total, the current study comprised 14 build cycles, spanning over a total build process time of around 500 hours, and initially involved 100 kg of virgin Alloy 718 powder that was loaded into the EBM machine before the start of cycle one. Hereafter, addition of fresh powder was kept as low as possible.

The CVN test samples with the dimension 11x11x60 mm were produced during each of cycle number 1, 6 and 14. Throughout the whole study, standard melt strategies and process parameters provided by the machine supplier were used for both contour and hatching exposure. The samples were built with the longitudinal axis parallel to the building direction. After EBM processing the samples were machined to the specified geometry as prescribed in ASTM standard E23-16b, illustrated in Fig.1. The notch was cut out using electrical discharge machining.

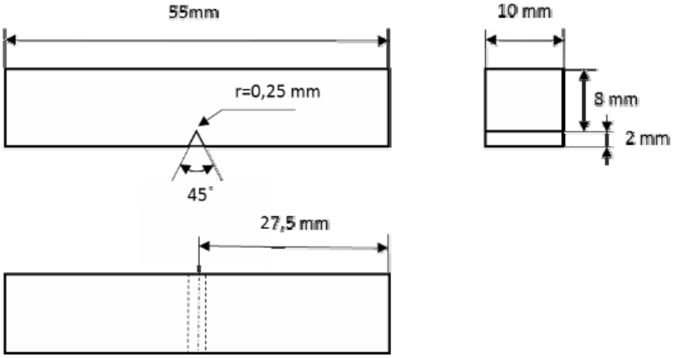

Fig.1. Charpy V-notch impact test sample geometry.

Between every build cycle the powder feedstock material was recovered according to the procedure specified by the machine manufacturer. Details on the powder recovery procedure can be found in for example Dehoff et al. [5] or in H. Gruber et al. [10]. For each of the build cycles, powder material from different positions within the building chamber was sampled for physical and chemical analysis. Detailed morphological analysis of the powder surface was performed using a Leo Gemini high resolution scanning electron microscope (HR SEM) equipped with an in-lens secondary electron detector. A solid state energy dispersive X-ray spectrometer (EDX) from Oxford Instruments (X-Max, Oxford Instruments Ltd., High Wycombe, UK) connected to the SEM was used for qualitative analysis of the phases present on the powder surface.

The CVN tests were performed on an Instron Wolpert PW30 impact tester with a capacity of 300 Joules. The test bars were tested and analyzed in as-built condition, without any subsequent heat treatment. Fracture surface analysis and metallography was done to study the fracture behavior and the presence of defects in test samples produced from powder feedstock material subjected to varying numbers of re-use cycles. Fracture surface analysis was performed using a Zeiss Discovery stereomicroscope supported by scanning electron microscopy and EDX for detailed analysis and micro-chemical analysis, respectively.

RESULTS AND DISCUSSION

Powder analysis

High-resolution scanning electron microscopy of the virgin and recycled powder was done to detect alterations in the powder surface chemistry and morphology connected to multi-cycle powder re-use. Representative surface morphologies of virgin and recycled powder are shown in Figure 2 and 3, respectively. In its virgin state, the powder generally consists of mostly spherical particles with a relatively clean appearance. Even though observed on relatively rare occasions, the virgin powder contains non-metallic inclusions, mainly Ti-rich nitride particles, being around a few µm in size (see Figure 2b). In general, however, the virgin powder surface shows only little presence of secondary phases and surface contamination, even at very high magnifications. However, already after the first build cycles, nano-sized secondary phase particulates start to form on the powder surface and tend to grow with increasing number of re-use cycles. After 14 build cycles, a considerable portion of the powder surface is covered by such particulates, as shown in Figure 3a. Even though their small size does not allow for quantitative chemical analysis by EDX, the clear enrichment in aluminum and oxygen as compared to the matrix material (see Table 2) indicate them as Al-rich oxide particles. A more detailed analysis of the powder material from a selection of the performed build cycles can be found elsewhere [10].

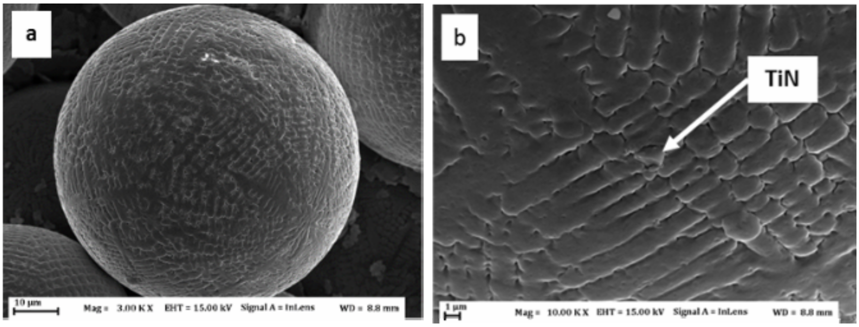

Fig.2. Surface morphology of the virgin powder.

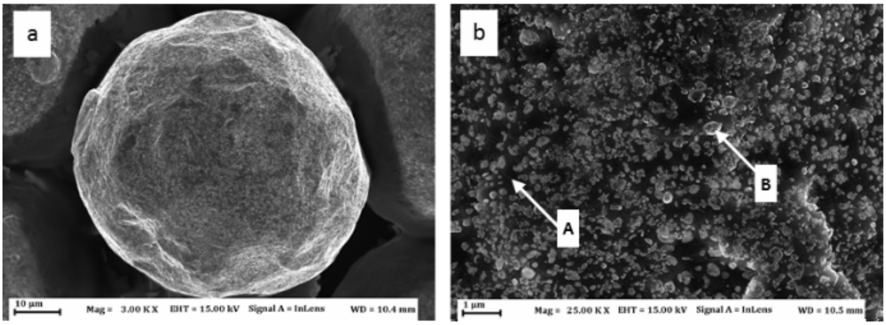

Fig.3. Surface morphology of the Alloy 718 powder after 14 re-use cycles. Corresponding EDX point analysis data are presented in Table 2.

Tab.2. EDX analysis data corresponding to analysis points in Fig.3b.

Location	Structure	Chemical composition								
			Ni	Cr	Fe	Nb	Mo	Ti	Al	O
A	Gamma matrix	wt.%	52.5	19.4	19.0	4.2	3.0	1.2	0.7	-
		at.%	51.6	21.5	19.8	2.6	1.8	1.4	1.4	
B	Aluminum-rich oxide	wt.%	36.7	15.3	14.5	3.6	2.0	1.5	13.2	13.2
		at.%	24.2	11.4	10.1	1.5	0.8	1.2	18.9	31.9

Fracture surface analysis

The fracture surface of a sample produced from virgin powder is shown in Fig.4a. On a macroscopic level, all investigated fracture surfaces had a similar overall appearance. They all showed only minor lateral expansion, which is an indication of a relatively brittle fracture. The fracture surface can be divided into two distinct regions – the core or bulk region of the sample, where a hatch exposure was performed, and the around 1 mm wide region along the surface edges which corresponds to the contour region (around 1,5 mm before machining). Macroscopically, the whole fracture surface is highly irregular and contains numerous ridges and depressions. Un-melted metal particles and secondary phases such as oxides were often observed in these sites, indicating damage initiation and crack front propagation along defect-containing weak interfaces. Similar observations have been done by, for example Deng et al. [8]. However, in that case presence of carbides and porosity was identified as a reason for the weak interfaces. At higher magnifications, as in Figure 5 and 6, it is realized that a large part of the areas close to and within the contour region consists of large, strikingly flat areas, partly covered with oxide films. As a consequence of the considerable amount of oxide phase on the surface of the re-cycled powder, the oxide covered areas in the samples produced from re-cycled powder (Fig.6) are significantly larger, as compared to the samples produced from virgin powder (Fig.5). Also in these areas, presence of un-melted powder particles and non-metallic phases indicate that many of these defects originate from both insufficient melting (lack of fusion) and/or weak bonding between non-metallic phases (oxide and nitride) and matrix material. Also in metallographic samples, larger sized defects preferentially located to the sample edges identify a high defect density close to or within the contour region, as shown in Fig.4b. In both cases, secondary phase particles such as Al-rich oxide and Ti-rich nitride are often spotted in the oxide-covered areas, as can be seen in Fig.5b. Corresponding qualitative chemical analysis measured by EDX analysis is presented in Table 3. The macroscopically rough topography in combination with the large fraction of defects suggests an intergranular type of failure, through crack propagation along weak interfaces, to be the main fracture mechanism close to or within the contour region. Due to the brittle nature evidenced by the widespread defect areas in this region, its contribution to the overall material toughness is most likely very small.

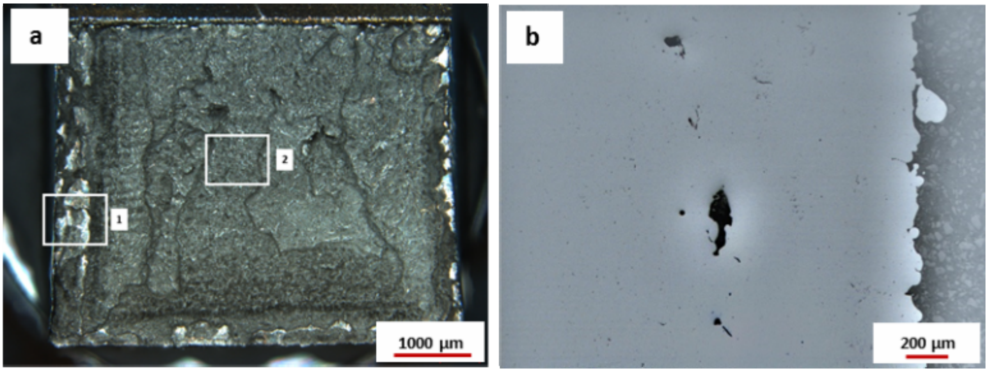

Fig.4. (a) Fracture surface of a CVN test sample produced from virgin powder. Denoted regions are further presented in Figs. 5 and 7, respectively. (b) Metallographic cross section of a sample produced from virgin powder showing large defects along sample edges.

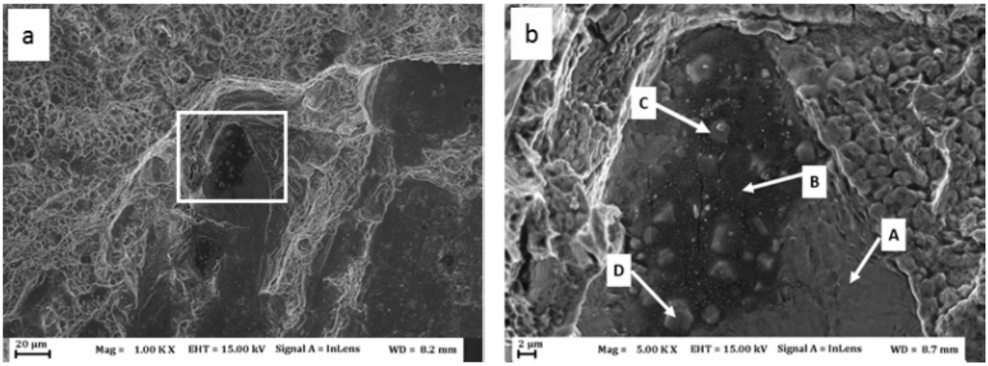

Fig.5. (a) Contour region on the fracture surface of a CVN test sample produced from virgin powder. (b) Higher magnification of denoted region showing oxide covered area with the presence of non-metallic particles. Corresponding EDX analysis data are presented in Tab.3.

Table 3. EDX analysis data from areas in Fig.5b.

Location	Structure	Chemical composition								
			Ni	Cr	Fe	Nb	Mo	Ti	Al	N	O
A	Gamma matrix	wt.%	51.6	18.7	19.2	5.3	3.1	1.3	0.8	-	-
		at.%	50.9	20.8	19.9	3.3	1.9	1.6	1.7		
B	Al-rich oxide film	wt.%	1.1	1.2	0.7	-	-	9.7	44.1	-	43.2
		at.%	0.4	0.5	0.3			4.4	35.6		58.8
C	Al -rich oxide particle	wt.%	10.7	5.4	4.1	5.0	-	10.8	31.7	-	32.3
		at.%	4.8	2.7	1.8	1.4		5.9	30.7		52.7
D	Ti-rich nitride particle	wt.%	1.8	0.7	0,7	5.0	-	74.2	0,6	13,4	3.4
		at.%	1.1	0.5	0.5	1.9		54.3	0.8	33.5	7.4

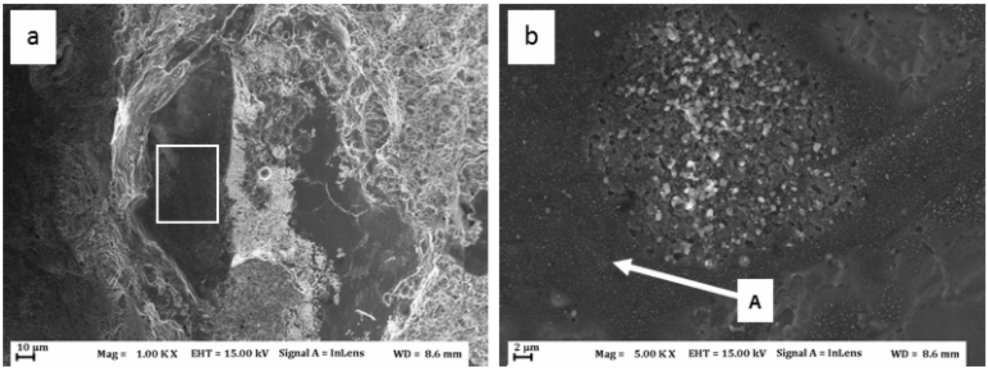

Fig.6. (a) Contour region on the fracture surface of a CVN test sample produced during cycle 14. (b) Higher magnification of denoted region showing oxide covered area. Composition in point A is almost identical to point B in Fig.5b.

Figure 7 shows the fracture surface in the hatching region of a sample produced from virgin powder. Generally, it consists of fairly equiaxed dimples, indicating ductile failure occurring through microvoid coalescence. Residual porosity, TiN and oxide particles, acting as micro-void nucleation sites were occasionally observed inside the dimples. In Figure 8, the corresponding images from a sample produced from recycled powder show presence of aluminum-rich oxide clusters (denoted area in Figure 8a) sizing up to around 50 µm. It is realized that the size and shape of the individual oxide particulates are very similar to the particulates observed on the recycled powder surface (Figure 3b). However, whether these particles are directly transferred from the powder feedstock or rather re-nucleated and clustered together in the melt pool has to be further elaborated. As already mentioned, weak bonding between oxide and metal and also different elastic properties may result in de-bonding and subsequent coalescence of the voids formed under tensile loading. Even though considerable amounts of defects were present in these samples, a major part of the fracture surfaces has dimple character. This shows that a considerable amount of plastic deformation took place during fracture, indicating an overall ductile fracture in a large portion of the sample. Anyhow, it is well known that that presence of agglomerates of non-metallic particles can have a significant negative effect on fatigue properties. Smaller sized agglomerates, similar to those observed in the hatch regions, may act as crack initiation sites in the high to very high cycle regime [11], whereas larger sized inclusions (preferentially observed close to the contour region) has been reported to be the main cause for fatigue life scattering in the low cycle regime [12]. Therefore, the larger amount of mainly oxide-containing defects in the samples produced from recycled powder shows that powder recycling may have a negative effect on the cleanliness and therefore also on the structural integrity of EBM processed Alloy 718, especially under dynamic loading. Hence, further research is needed to increase the knowledge about imperfections in AM built components, concerning both defect formation and their effects at different loading conditions, preferably using more sophisticated techniques such as fracture toughness and/or fatigue testing.

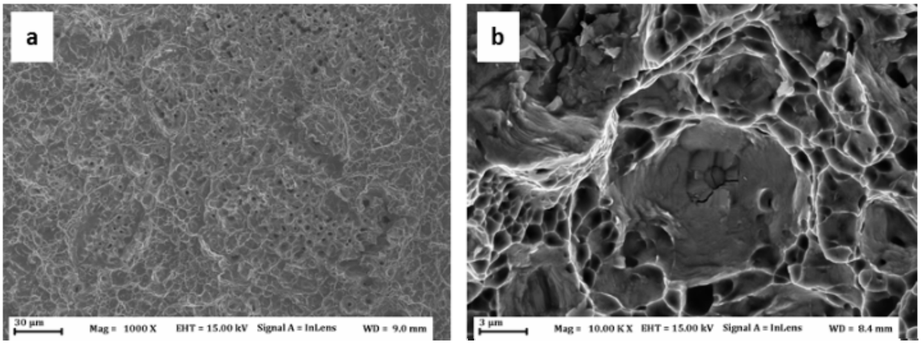

Fig.7. Hatching region on the fracture surface of a CVN test sample produced from virgin powder.

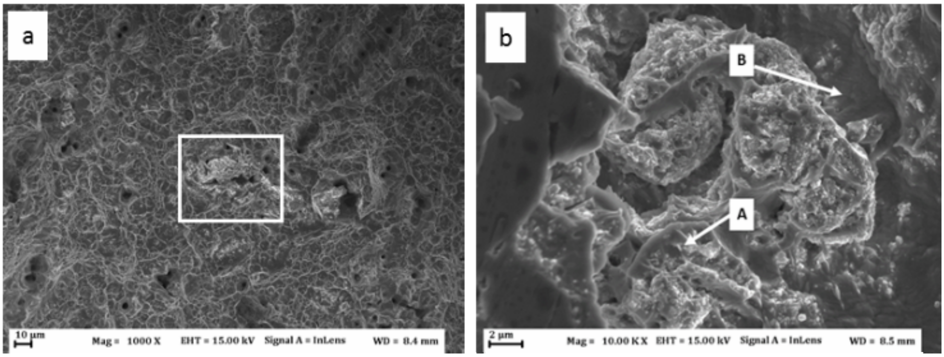

Fig.8. (a) Hatching region on the fracture surface of a test sample produced during cycle 14. (b) Higher magnification of denoted region showing aluminum rich oxide cluster. Corresponding EDX analysis data are presented in Table 4.

Tab.4. EDX analysis data from the areas in Fig.8b.

Location	Structure		Chemical composition,							
			Ni	Cr	Fe	Nb	Mo	Ti	Al	O
A	Aluminium-rich oxide	wt.%	19.4	8.5	7.9	3.4	2.1	2.1	25.5	31.2
		at.%	9.1	4.5	3.9	1.0	0.6	1.2	26.1	53.7
B	Gamma matrix	wt.%	51.8	19.4	19.4	4.7	2.8	0.9	1.0	-
		at.%	50.7	21.4	20.0	2.9	1.7	1.1	2.1	

CONCLUSIONS

Fracture surface analysis of EBM processed Alloy 718 Charpy impact test bars produced from virgin and multi-cycle re-used powder was performed to study the effect of process induced powder degradation on defect formation and fracture behavior. The findings can be summarized as follows:

- A considerable amount of defects of varying type and size was present in samples produced from both virgin and recycled powder.

- A large heterogeneity in terms of fracture features was observed across the fracture surfaces, with larger sized defects being preferentially located to areas close to or within the contour region.
- A large part of the areas close to or within the contour region showed presence of an intergranular type of fracture along weak interfaces originating from insufficient melting and/or presence of Al-rich oxide films and non-metallic inclusions. The main fracture mode in the hatch region was a moderately ductile dimple fracture.
- The areas covered by oxide films were significantly larger in the samples produced from recycled powder as compared to the samples produced from virgin powder.
- Al-rich oxide particle clusters in the hatching region were exclusively found in components produced from recycled powder.

Acknowledgement

The authors would like to acknowledge SIP LIGHTer and the Swedish Innovation Agency Vinnova as well as AoA Production at Chalmers for financial support. The authors express appreciation to Jonas Olsson at Production Technology Center, Trollhättan, Sweden for providing the samples.

REFERENCES

[1] Strondl, A., Palm, M., Gnauk, J., Frommeyer, G.: Mater. Sci. Technol., vol. 27, 2011, no. 5, p. 876
[2] Chlebus, E., Gruber, K., Kuznicka, B., Kurzac, J., Kurzynowski, T.: Mater. Sci. Eng. A, vol. 639, 2015, p. 647
[3] Ma, X., Duan, Z., Shi, H., Murai, R., Yanagisawa, E.: J. Zhejiang Univ. A, vol. 11, 2010, no. 10, p. 727
[4] Ardila, LC., Garciandia, F., González-Díaz, JB., Álvarez, P., Echeverria, A., Petite, MM. Deffley, R., Ochoa, J.: Phys. Procedia C, vol. 56, 2014, p. 99
[5] Dehoff, RR., Kirka, MM., Sames, WJ., Bilheux, H., Tremsin, AS., Lowe, LE., Babu, SS.: Mater. Sci. Technol., vol. 31, 2015, no. 8, p. 931
[6] Denda, T., Bretz, PL., Tien, JK.: Metall. Trans. A, vol. 23, 1992, no. 2, p. 519
[7] Riemer, A., Leuders, S., Thöne, M., Richard, HA., Tröster, T., Niendorf, T.: Eng. Fract. Mech., vol. 120, 2014, p. 15
[8] Deng, D., Moverare, J., Peng, RL., Söderberg, H.: Mater. Sci. Eng. A, vol. 693, 2017, p. 151
[9] Sames, V., William James: Additive manufacturing of Inconel 718 using electron beam melting: Processing, post-processing, & mechanical properties, 2015, p. 340
[10] Gruber, H., Hryha, E., Nyborg, L.: Alloy 718 powder degradation during multi-cycle EBM processing. In manuscript
[11] Krewerth, D., Lippmann, T., Weidner, A., Biermann, H.: Int. J. Fatigue, vol. 84, 2016, p. 40
[12] Matz, JE., Eagar, TW.: Metall. Mater. Trans. A, vol. 33, 2002, no. 8, p. 2559

Powder Metallurgy Progress, Vol.18 (2018), No.1, p.049-057
http://dx.doi.org/10.1515/pmp-2018-0006

INVESTIGATING THE MICROSTRUCTURAL AND MECHANICAL PROPERTIES OF PURE LEAD-FREE SOLDERING MATERIALS (SAC305 & SAC405)

P. Manoj Kumar, G. Gergely, D. K. Horváth, Z. Gácsi

Abstract
The Sn–Ag–Cu (SAC) solders with low Ag or Cu content have been identified as promising candidates to replace the traditional Sn–Pb solder. In this study, an extensive discussion was presented on two major area of mechanical properties and microstructural investigation of SAC305 and SAC405. In this chapter, we study the composition, mechanical properties of SAC solder alloys and microstructure were examined by optical microscope and SEM and mechanical properties such as tensile tests, hardness test and density test of the lead solder alloys were explored. SAC305 and SAC405 alloys with different Ag content and constant Cu content under investigation and compare the value of SAC305 and SAC405. From this investigation, it was reported that tensile strength is increased, with an increase of Ag content and hardness and density were also increases in the same manner.

Keywords: Lead-free solder, Sn–Ag–Cu alloys, Microstructure, Mechanical properties

INTRODUCTION

Soldering is the most important joining process in the electronics industry. To the environmental concerns and health hazards associated with Pb-Sn solders, several studies have been focused on lead-free solder alternatives [1]**.** It is important to ensure that the thermal, mechanical and physical properties of lead-free solders are superior to those of Sn-Pb solders. Since the portable electronic products increased to high speed, light weight, continual miniaturization and multi-functionality of integrated circuits, the transition to Pb-free solders occurred to compact with the increase in portable electronic products. So in the reliability condition, both the thermal cycling loading and drop performance are important for portable electronic products. The most important for electronic industry appears to be the Sn-Ag-Cu (SAC) alloys eutectic or near eutectic alloy system. These alloys can offer an excellent combination of better thermal, mechanical and wettability compared to Pb-Sn solders. Moreover, the SAC solders alloys have a good quality joint with different substrates, i.e chip scale package as well as ball grid array (BGA) interconnect. The main reason for weak mechanical properties of solder joint is the large formation of Ag_3Sn and Cu_6Sn_5 IMC, so these problems need to be resolved. For that reason, the industries mostly use the low-Ag SAC solder alloys such as SAC105, SAC205 and, SAC305, which have low cost and better performance than eutectic or near-eutectic SAC alloys in drop impact reliability [1, 7].

Manoj Kumar Pal, Gréta Gergely, Dániel Koncz Horváth, Zoltán Gácsi: Faculty of Materials Science and Engineering, Institute of Physical Metallurgy, Metal forming and Nanotechnology, University of Miskolc, Hungary

With the requirement of lead-free solders, it is necessary to understand that how different lead-free solders affect the reliability of microelectronic assembly when subjected to different loading conditions such as thermal cycling, bending, vibration and drop impact. The Sn–Ag–Cu solder is one commonly used lead-free solder in surface mount technology (SMT) assembly for microelectronics. Many studies were conducted on Sn–Ag–Cu lead-free solders. Results showed that the Ag content affects the mechanical properties and microstructures with Sn–xAg–Cu lead-free solder joint [2, 7].

Pb-free solders are good alternatives to traditional Sn-Pb solders alloys and their existence are great efforts in course. The traditional Sn–Pb solder alloy is the dominant solder material in the industry because of their very low melting temperature.

In the context of the environmental and human precaution, Sn-Pb has not been widely promoted. Since 2006 the environmental protection agencies (RoHS and WEEE) have banned the lead-containing portable electronic products because lead and lead-containing products are toxic substances and it would be very harmful to the well-being of humans and the environment. So the researchers are trying to find the other alternatives without Pb and lead-free solders are good alternatives because lead-free solders are non-toxic [3, 8].

Sn–Ag alloys have three different Ag_3Sn morphologies during solidification. Various researchers have been shown IMCs i.e. Spheroids, needles and platelets type intermetallic (Ag_3Sn) particles. Regarding the mechanical strength, the Ag_3Sn IMC is brittle in nature when compared with the Sn-rich matrix. Under stressed loading conditions, serious problems can be carried by the brittle nature of the Ag_3Sn intermetallic. It has been described that Sn–Ag solder having a coarse dendritic microstructure with fiber-platelets like Ag_3Sn particles has lower corrosion resistance when compared with that of the same alloy having a microstructure characterized by finely and homogeneously distributed spheroids like fiber Ag_3Sn IMC particles. The aim of this paper is to develop a comparative analysis of the mechanical properties of different lead-free solder alloys with those of the traditional Sn–Pb alloy. Experimental results characterizing the microstructural and mechanical properties of SAC305 and SAC 405 alloys. These two SAC solder alloys have been selected due to two main reasons: (i) to determine the effect of silver content on the microstructure and mechanical behavior and (ii) these alloys have been subjected a contradiction in the research [8].

For higher density packages, flip-chip interconnects are increasingly used in daily life. Eutectic Sn-Pb alloy is one of the most popular solders used in flip chip today. Lead-free solder balls are environmentally friendly technology at this time for the electronics industry. Many researchers have been proposed for lead-free solders for material characteristics in manufacturing, reliability, and performance, such as melting temperature, solderability, cost, and long-term reliability. As SAC solders (3 to 4 wt% of Ag) having lower melting points and good solderability with good reliability, these solders are the primary lead-free solder compositions for flip-chip solders [4, 9].

In the electronics industry, the solder joint reliability is a great concern under thermal and mechanical loading. For the reliability assessment, reliability testing and computational modeling are common methods. Compare to actual reliability tests, the modeling is more efficient than actual, which are time-consuming, expensive, and require a more manpower for failure analysis and measurement.

The material properties of the solder joint are needed for modeling. Therefore, for a reliable numerical model, it is very important to characterize material properties accurately. Various researchers have been reported on the characterization of mechanical properties of lead-free solders and lead solders. Tensile and compressive tests are the conventional techniques used for characterization. Compare to the bulk solder bars, the material properties of the small solder joints are different which used in electronics assembly because they have different microstructures and different intermetallic compound layers. It is necessary to perform characterization on actual solder joints for the effects of microstructures and intermetallic compound distribution. For the characterization of mechanical properties of actual solder joints, the conventional techniques, nanoindentation can be used. But these techniques provide only the properties of the individual phases in the solder joints and does not provide a value for the Poisson's ratio [5, 10].

In recent years, the portable electronics products are highly demanded because of the shrinking in size of electronic components and solder joint dimensions. Furthermore, by the government legislation, the electronics industry has been adopted to lead-free solders due to environmental and health concerns issues from the use of Pb-based solders. In the recent time, several lead-free solders have been developed such as Sn-Bi, Sn-Ag, Sn-Cu, and Sn-Ag-Cu alloys. Sn-Ag-Cu (SAC) is nontoxic solder alloy and it has good mechanical properties and wettability. It the most widely used lead-free solders this time. However, according to the literature, Sn-Pb solders are less brittle in nature than SAC solder alloys with high Ag content because, in SAC solder, the intermetallic compounds (IMC) Ag_3Sn IMC formed at the SAC solder/Ag interface and Cu_6Sn_5 and Cu_3Sn are formed at the SAC solder/ Cu interface. In addition, the high Ag content SAC solder increases the cost of the products compared to the low Ag content SAC solder alloy. Thus, it is mandatory to choose the low-Ag-content SAC alloys. Reducing the Ag content can improve the reliability of SAC solder joints in dynamic environments. It has been proved that to further enhance the properties of SAC solder alloys, alloying elements such as Sic, Bi, Ni and, Ce have been added in lead-free solder alloys [3, 6, 11].

EXPERIMENTAL PROCEDURES

Before the start, the experiment, composition of lead-free solder had to check by the inductively coupled plasma mass spectrometry (ICP-MS). Table1 shown the composition of SAC305 and SAC405 which provided by the HENKEL and also checked by inductively coupled plasma mass spectrometry (ICP-MS).

Tab.1. Composition of SAC305 and SAC405 provided by HENKEL (wt %).

Alloy name by Henkel	Sn	Ag Henkel	Ag ICP	Cu	Cu Henkel	Cu ICP
SAC305	96.5	2.9524	3.03	0.5	0.5955	0.76
SAC405	95.5	3.9918	3.81	0.5	0.5992	0.52

Five specimens had to be cast of SAC 305 and SAC 405 and furnace temperature was 400°C. These specimens had to be cast at room temperature and holding time was 45 minutes in the furnace. The solder alloys were melted in the furnace and maintained 100°C above their respective melting point for 45 minutes. The solder specimens were cast inside the designed mold. Then, the specimens were naturally air-cooled at room temperature. The specimen was annealed at 100°C for 2 h to reduce the residual stress, induced in the sample preparation before the testing. Then, the solder bars were fixed onto a testing grip at two ends of a specimen using a universal testing machine.

Tensile tests were conducted on bulk solder cylindrical dog bone SAC305 and SAC405 solder specimens. Figure 1 shown, the dog-bone-shaped bulk solder specimens for the uniaxial tensile test were prepared by machining from casted lead-free solder bar

SAC305 and SAC405. The specimens had a total length of 60 mm and a gage length of 30 mm. The diameter of the gage length was 5mm.

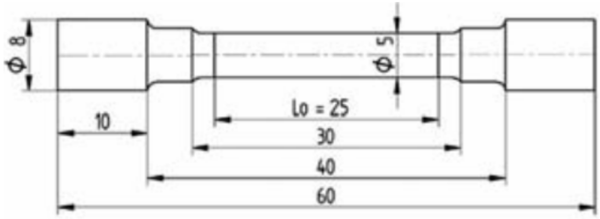

Fig.1. Dog-bone-shaped tensile test specimen.

This paper focuses on the effect of Ag content and the mechanical material properties of lead-free solders. Five samples were tested under the same testing condition for each specimen to obtain the reliable and repeatable results. Then, the mechanical properties were obtained by averaging testing data. The tensile tests were conducted at room temperature (25°C) for SAC305 and SAC405. The microstructures of solders (SAC305 and SAC405) were investigated based on the microscope and scanning electron microscope (SEM) images. The SEM samples were prepared by dicing, resin molding, grinding and polishing processes. The effects of Ag content on IMCs (Ag_3Sn and Cu_6Sn_5) distribution and Sn dendrite were examined to understand the effect of Ag content on the mechanical properties of solders.

RESULTS AND DISCUSSION

Effect of strain on solder mechanical properties

Figure 2 shows the ductile failure mode of SAC305 and SAC405 solder alloys. Necking and surface coarsening analysis were analyzed for the tested solder before complete failure.

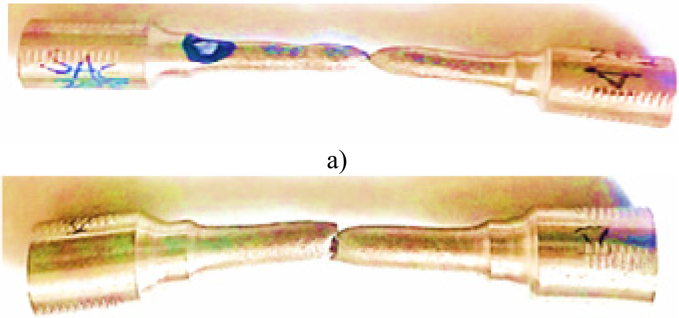

a)

b)

Fig.2. Typical ductile failure of (a) SAC305 and (b) SAC405 solder.

The tensile stress–strain curves of Sn–3.0Ag–0.5Cu and Sn–4.0Ag–0.5Cu solder alloys are shown in figure 2(a) and figure 2(b). The strain affects the mechanical properties significantly. The solder has been effected on the ductility with large elongation and plastic deformation before fracture. UTS and elongation increase with increasing tensile strain.

Effect of Ag content on solder mechanical properties and microstructures

Figure 3 shows the stress–strain curves for SAC305 and SAC405 solders under the same loading conditions. The Figure shows also that the tensile strength of solder increases with increasing the Ag content but ductility reduces when the Ag content increases in Sn–Ag–Cu solder. Therefore, high Ag content solder joint has lower drop lifetime in the electronic assembly when subjected to drop impact, which is the testing results given by Amagai et al. [12]. The low Ag content solders are mainly used in the portable electronic assembly for handheld electronic products to improve the drop performance of solder joint [12, 13].

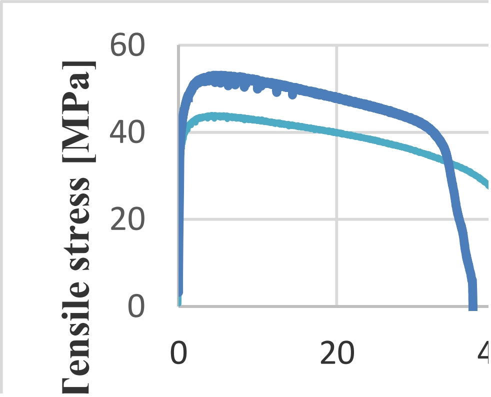

Fig.3. Effect of Ag content on the stress–strain curves of SAC305 and SAC405 solders.

Microstructural characterization of solder

The microstructure of the SAC305 (Sn-3.0Ag-0.5Cu) and SAC405 (Sn-4.0Ag-0.5Cu) solders having a Sn matrix phase where Ag_3Sn needles-like and Cu_6Sn_5 in the bulk form are uniformly distributed in an Sn rich phase. In order to investigate the effect of Ag content on the solder mechanical properties and microstructures by the scanning electron microscopy and microscope were used to study the microstructures of lead-free solders. Figure 4 and 5 shows the SEM images and microscopic images of microstructure for different Sn–Ag–Cu solders. It can be seen that the Ag content affects the Ag_3Sn and Cu_6Sn_5 intermetallic compound (IMC) precipitate. In Sn–Ag–Cu solder amount of Ag_3Sn and Cu_6Sn_5 IMCs increases when the Ag content increases and distributed in a Sn-rich matrix. Therefore, finer Sn dendrites have been seen in the microstructure of solder which has the higher Ag content and more IMC precipitates in solder with higher Ag content such as SAC405.

The typical example of low and high-magnification SEM microstructure of SAC305 and SAC405, alloy of IMC phases are shown in Fig.5. The show the microstructures of SAC305 and SAC405 consists of β-Sn dendrites and mixture of Ag3Sn and Cu_6Sn_5 IMCs distributed within Sn-rich matrix. Similar microstructures were reported in other SAC studies [11]. In Figure 4 and 5, the needle-like particles are identified as Ag_3Sn IMCs, whereas an irregular polygon of IMC particles are Cu_6Sn_5. These large IMCs (Ag3Sn and Cu_6Sn_5) particles are present in near eutectic lead-free solders, and could lead to failure due to the high interfacial energy between the solid solder and IMCs particles [15].

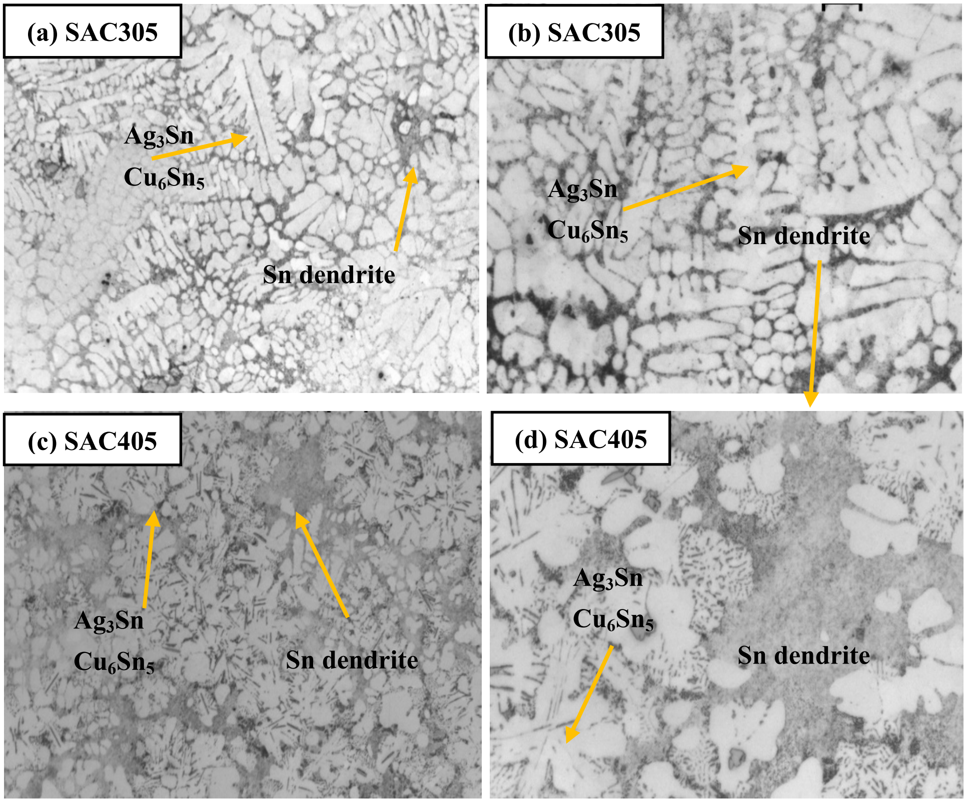

Fig.4. Low and high magnification microstructures of SAC305 (a, b) and SAC405 (c,d).

Melting behavior

Alloys having low silver content have two distinct melting phases. One is Sn-Ag eutectic and second is high-temperature phase corresponding to Sn-Cu eutectic. The melting temperature of the SAC305 and SAC405 solders were determined by DSC analysis. The Sn-Ag3.0-Cu0.5 and The Sn-Ag4.0-Cu0.5 solder were found to have a melting interval of 215-220°C and 217-219°C.

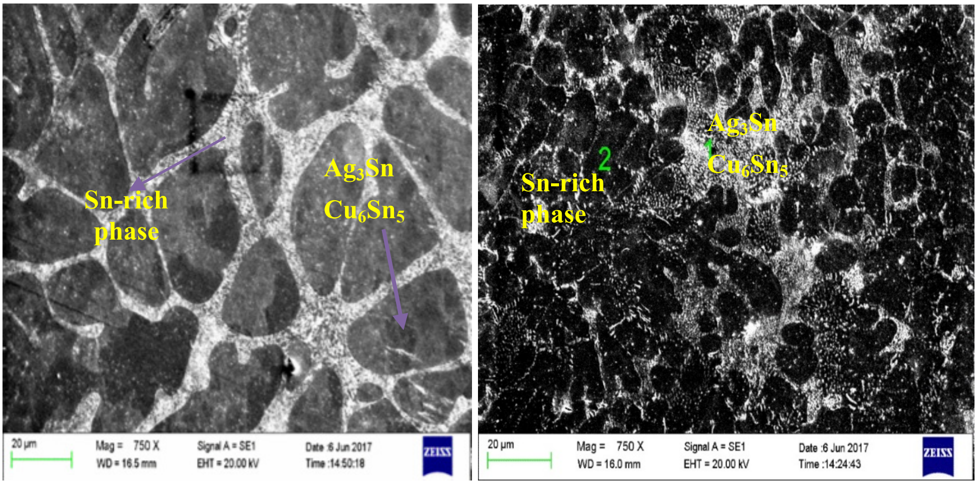

a) b)

Fig.5. SEM images of the microstructure of Sn–Ag–Cu solders: (a) SAC305 and (b) SAC405.

General tensile and hardness test

The tensile properties of SAC305 and SAC405 solder alloys are mainly controlled by their microstructures, which depend on the amount of Ag content, shape and size of IMC particles and their distribution in alloy matrix. Figure 6, Figure 7 and Table 2 compare the tensile properties and hardness properties of plain SAC207 solder.

Tab.2. Tensile and hardness properties of the solders SAC305 and SAC405.

Alloy	Hardness (HV)	Tensile strength (MPa)
SAC305	13.47	40.95
SAC405	13.98	43.70

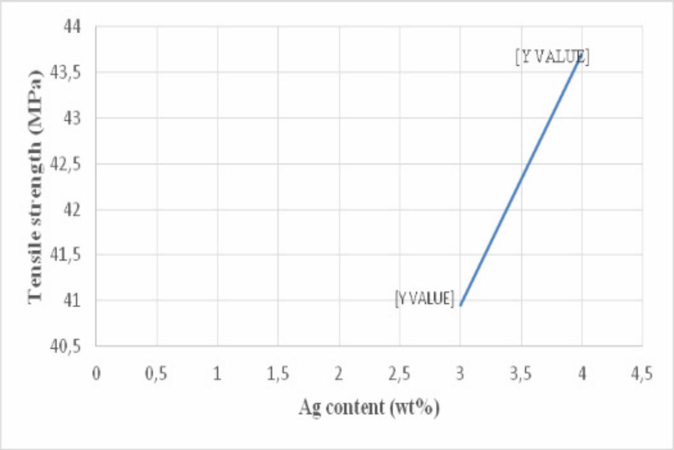

Fig.6. Comparative tensile curves for SAC305 and SAC405 solder alloys.

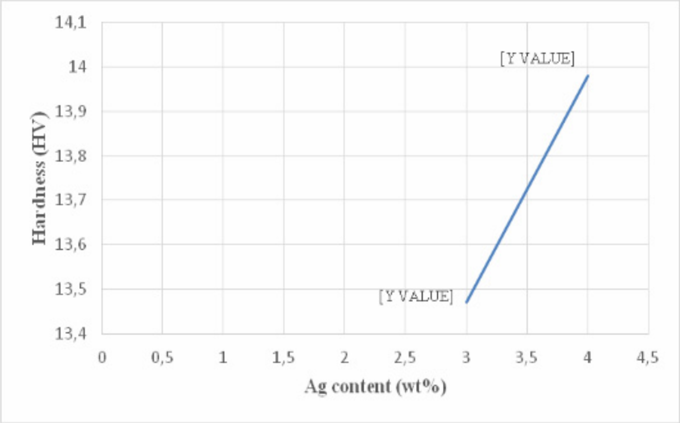

Fig.7. Comparative hardness curves for SAC305 and SAC405 solder alloys Figure caption.

Figure 6 and Figure7 shown that the tensile strength of SAC405 is higher than SAC305 and hardness of SAC405 is higher than SAC305. Ag content is a basic reason for these mechanical properties.

CONCLUSION

Silver content is very important for the soldering process and solder joint reliability. Based on the present investigations described in this work, several conclusions may found regarding a comparative evaluation of microstructural and mechanical deformation behavior of SAC305 and SAC405 solders. In this study, an extensive discussion has been presented on two major area of mechanical properties and microstructural investigation of SAC305 and SAC405. From this present experimental investigation, the following main conclusions can be drawn:

1. Microstructures were examined by optical microscope and SEM images. Needle-like Ag_3Sn and Cu_6Sn_5 intermetallic compound (IMC) precipitate were found and saw in Sn–Ag–Cu solder amount of Ag_3Sn and Cu_6Sn_5 IMCs increases when the Ag content increases and distributed in a Sn-rich matrix. Therefore, finer Sn dendrites were seen in the microstructure of solder which has the higher Ag content and more IMC precipitates in solder with higher Ag content such as SAC405.
2. Melting interval of the SAC305 and SAC405 solders were determined by DSC analysis. The Sn-Ag3.0-Cu0.5 and The Sn-Ag4.0-Cu0.5 solder were found to have a melting interval of 215-220°C and 217-219°C.
3. The tensile strength of SAC305 is 40.95 MPa and SAC405 is 43.70 MPa which is higher than SAC305 and hardness of SAC305 is 13.47 HV and SAC305 is 13.98 HV which is higher than SAC305.

REFERENCES

[1] El-Daly, AA., El-Hosainy, H., Elmosalami, TA., Desoky, WM.: Journal of Alloys and Compounds, 2015, p. 402
[2] El-Daly, AA., Al-Ganainy, GS., Fawzy, A., Younis, MJ.: Materials & Design, vol. 55, 2014, p. 837
[3] El-Daly, AA., Fawzy, A., Mansour, SF., Younis, MJ.: Materials Science and Engineering A, vol. 578, 2013, p. 62
[4] Nai, SML., Wei, J., Gupta, M.: Thin Solid Films, vol. 504, 2006, no. 1-2, p. 401

[5] Liu, P., Yao, P., Liu, J.: Journal of Electronic Materials, vol. 37, 2008, no. 6, p. 874
[6] Tang, Y., Li, GY., Pan, YC.: Materials & Design, vol. 55, 2014, p. 574
[7] Che, FX., Zhu, WH., Poh, ES., Zhang, XW., Zhang, XR.: Journal of Alloys and Compounds, vol. 507, 2010, no. 1, p. 215
[8] Osório, WR., Leiva, DR., Peixoto, LC., Garcia, LR., Garcia, A.: Journal of Alloys and Compounds, vol. 562, 2013, p. 194
[9] Terashima, S., Kariya, Y., Hosoi, T., Tanaka, M.: Journal of Electronic Materials, vol. 32, 2003, no. 12, p. 1527
[10] Nguyen, TT., Yu, D., Park, SB.: Journal of Electronic Materials, vol. 40, 2011, no. 6, p. 1409
[11] Hammad, AE., El-Taher, AM.: Journal of electronic materials, vol. 43, 2014, no. 11, p. 4146
[12] Amagai, M., Toyoda, Y., Tajima, T. In: Proceedings of Electronic Components and Technology Conference, 2003, p. 317
[13] Zhu, WH., Xu, L., Pang, JH., Zhang, XR., Poh, E., Sun, YF. Tan, HB. In: Electronic Components and Technology Conference, 2008. ECTC 2008, p. 1667
[14] Hamada, N., Uesugi, T., Takigawa, Y., Higashi, K.: Journal of Alloys and Compounds, vol. 527, 2012, p. 226
[15] Mayappan, R., Yahya, I., Ab Ghani, NA., Hamid, HA.: Journal of Materials Science: Materials in Electronics, vol. 25, 2014, no. 7, p. 2913

Powder Metallurgy Progress, Vol.18 (2018), No.1, p.058-069
http://dx.doi.org/10.1515/pmp-2018-0007

ENAMEL REMINERALIZATION POTENTIAL OF NOVEL DENTIFRICE WITH TETRACALCIUM PHOSPHATE/MONETITE POWDER COMPONENT

L. Medvecky, R. Stulajterova, M. Giretova, J. Mincik, M. Vojtko, J. Balko, E. Petrovova

Abstract

The aim was to investigate the enamel health benefits of a novel toothpaste with active tetracalcium phosphate/monetite mixtures under de/remineralization cycling .The enamel de/remineralization cycling protocol was consisted of demineralization in 1% aqueous solution of citric acid at pH 3.6 with following treatment with toothpastes and soaking in remineralization storage solution. Effectiveness of toothpastes to promote remineralization was evaluated by surface microhardness measurements, enamel erosion depth, analysis of surface roughness and fluorescent optical method. The novel tetracalcium phosphate/monetite toothpaste had the same remineralization potential as commercial calcium silicate/phosphate toothpaste and significantly higher than control storage solution group ($p<0.05$). Surface roughness was significantly lower after addition of fluorides to dentifrice ($p<0.05$). The enamel erosion depth was significantly reduced by applying toothpastes as compared to negative control ($p<0.05$) and did not differ from calcium silicate/phosphate toothpaste ($p>0.66$). The results showed that dentifrice formulations containing active tetracalcium phosphate/monetite mixture with or without fluoride addition had excellent enamel remineralization potential under de/remineralization cycling and successfully promote remineralization of enamel with daily using in the form of toothpaste.

Keywords: dentifrice, enamel, fluoride, remineralization, demineralization

INTRODUCTION

Dentifrices represent widely used and effective tool for preventing the development of caries with ability to promote of enamel or dentin remineralization in dependence on their composition. The regular brushing of the teeth with a fluoride toothpaste can reduce the incidence of dental caries and fluoride ions can be delivered to the tooth surface, saliva and other tissues including plaque biofilm. In the case of the formation of fine CaF_2 – like deposits on enamel surface these can act like fluoride reservoir for the protection of enamel hydroxyapatite or fluorohydroxyapatite to dissolution [1].

Lubomir Medvecky, Radoslava Stulajterova, Maria Giretova, Marek Vojtko, Jan Balko: Institute of Materials Research of SAS, Watsonova 47, 040 01 Kosice, Slovakia
Jozef Mincik: Private Dental Practice,Vystavby 3, Kosice, Slovakia
Eva Petrovova: Institute of Anatomy, University of Veterinary Medicine and Pharmacy in Kosice, Komenskeho 73, Kosice, Slovakia

The effectivity of toothpaste for promoting enamel health can be enhanced by the addition of calcium and phosphate compounds. The delivery of calcium and fluoride ions and the increase of plaque calcium concentration is one of possible ways to prevent demineralization by the rise in the cariostatic activity of toothpaste. The generally utilized phosphate and fluoride compounds in toothpaste composition represent sodium phosphate, calcium phosphates (brushite, amorphous calcium phosphates, casein phosphopeptide-stabilized amorphous calcium phosphate (CPP-ACP), functionalized β-tricalcium phosphate (fTCP), nanohydroxyapatite, organophosphates), sodium monofluorphosphate, calcium glycerol phosphate, NaF, amine fluoride and compounds of Zn, Sr or Sn [2-6]. Another large group of highly effective toothpastes with anti-caries protection and remineralization potential is based on calcium silicates, calcium silicate/phosphates or bioglass (NovaMine™) and dual phase gel treatment with ability to improve the formation of nanohydroxyapatite coating on enamel or dentin surfaces [7-12]. It was revealed that the calcium silicate/phosphate deposits onto enamel surfaces supported formation of hydroxyapatite crystalline phases close to the enamel mineral hydroxyapatite [13]. It has been found the comparable remineralization effect (even in depth) of the calcium glycerolphosphate (CaGP)/fluoride toothpaste on enamel at lower content of fluorides (500 ppm F^-) as in commercial 1100 ppm F^- fluoride paste [14]. Strong enamel remineralization was found by applying of chewing gum with CPP-ACP component [15] and rinses containing 450 ppm F^- or 225 ppm F^- with a small amount of fTCP [16]. On the other hand no differences on reduction of artificial caries lesions were identified in in-situ study between CPP-ACPF, fTCP and fluoride pastes despite of a significant reduction in lesion area [17].

The commercial fluoride-free $ZnCO_3$/nanohydroxyapatite dentifrices had higher remineralizing effect than pure amine fluoride [18] but a low in vitro inhibition of caries demineralization was observed using the fluoride-free nanohydroxyapatite containing toothpastes [19]. Nanohydroxyapatite was used practically in the form of aqueous slurries directly applied on eroded enamels or admixed into acid drinks' [20-22]. The addition of nanohydroxyapatite especially to acid suspension caused supersaturation of saliva in relation to hydroxyapatite or fluorohydroxyapatite with following precipitation of fine calcium phosphate coating. On the other hand, the more active dentin desensitizer based on fluoride-free powder tetracalcium phosphate/monetite mixtures (TEETHMATE® desensitizer) has been developed and it have to be applied on tooth surface in the form of slurries in phosphate solution. The advantage of above solution can be in higher activity of calcium phosphates because of the gradual hydrolysis and fast mutual interaction between components with the formation of calcium deficient hydroxyapatite. A lower effectivity of TEETHMATE® (Kuraray Noritake Dental, Tokyo, Japan) desensitizer than Nanoseal® (Nippon Shika Yakuhin, Yamaguchi, Japan) desensitizer with fluoro-alumino-calcium silicate glass component was found as the result of the formation of a more stable fluoroapatite and silica on bovine dentin [23].

The aim of this paper was to develop simply applicable dentifrices with active tetracalcium phosphate/monetite mixture and to evaluate their enamel remineralization properties under de/remineralization cycling. The prepared toothpastes differenced by morphology or particle size of monetite phase from the TEETHMATE® powder component (microcrystalline tetracalcium phosphate/monetite mixture (micTTCPM)), which was used and compared with in situ prepared mixture containing the nanomonetite phase (TTCPM) with the same Ca/P ratio as in commercial micTTCPM powder. In the next, the effect of fluoride addition (1450 ppm F^- as NaF) to TTCPM dentifrice (TTCPMF) on the surface hardness recovery and microstructure of enamel surface was studied. Besides, the prepared toothpastes were compared with both the commercial dentifrice (SENSODYNE®, GlaxoSmithKline) containing calcium sodium phosphate/silicate and 1450 ppm F^- as positive control and remineralization solution treated enamels as negative control.

MATERIALS AND METHODS

Experimental dentifrices

Experimental toothpastes were prepared using carboxymethylcellulose, glycerol, amorphous silica, sodium lauryl sulfate, sorbitol, xylitol, calcium phosphate mixture, NaF (in the case of fluoride pastes) and water. Tetracalcium phosphate/nanomonetite mixture was prepared according to Medvecky et al. (2015) [24]. The fluoride content in TTCPMF paste was 1450 ppm (NaF, analytical grade, Sigma-Aldrich) and NaF was before using refined by re-precipitation after dissolution in distilled water and following fast addition of ethanol (absolute, analytical grade, Reag,Pharm.Eur, Merck). The commercial microcrystalline tetracalcium phosphate/monetite powder mixture (micTTCPM) was used without any further treatment. SENSODYNE® dentifrice (CaPSi) was composed of calcium sodium phosphate/silicate, 1450 ppm F^- as sodium monofluorphosphate, glycerin, PEG8, hydrated silica, sodium lauryl sulfate, titanium dioxide, carbomer, sodium saccharin, eugenol, limonene.

Sample preparation

The teeth used in experiment were extracted for orthodontic reasons and with the informed consent of patients (protocol No: 088/2005- PH/CEP). Crowns from freshly extracted human non-carious molars were sectioned from the roots horizontally and then vertically to obtain their buccal surfaces using a slow speed diamond disk attached to the micro-motor under water lubrication. The specimens were then embedded in self-cured two component epoxy resin (3M). The buccal/lingual surfaces were wet ground using 800, 1200, 2400 and 4000-grit water proof silicon carbide paper (Struers) to obtain a smooth flat surface. The one halve of each flat enamel surface was coated with the water resistant nail varnish and was used as baseline for the evaluation of properties. Uncoated area of enamels (2x2 mm) was utilized as sample for treatment with dentifrices. Samples were soaked in physiological solution (0.9 % NaCl) until using.

Surface microhardness analysis and surface roughness

The surface microhardness was measured using microhardness tester (TUKON 1102, Wilson Hardness) with a Vickers indenter at 25 g load for 15 s. Six indentations per test were performed on each specimen and the mean and standard deviation was taken. The surface hardness of the polished sound enamel (VHM_s) was measured as baseline after removing of varnish. The final VHM_f characterizes surface enamel microhardness after 10 de/remineralization cycles. The surface microhardness recovery ΔVMH was calculated as $\Delta VMH = (VHM_s - VHM_f)/VHM_s) \times 100$.

The surface roughness (S_a) of samples (5 samples of each group) was measured by the 3D optical profilometer (PLu Neox Sensofar, Spain) in a confocal mode with 200× objective (NA 0.95, maximum slope 71°, vertical resolution <1 nm). The image analysis was done using the SensoMap standard software. The enamel erosion depth of samples (5 samples of each group) was calculated from profilometer line scans as the average distance (Δh) between surface of polished sound enamel and enamel surfaces after 10 de/remineralization cycles (mean of three depth line profiles on each sample).

XRD phase analysis, SEM and optical fluorescent microscopy

The phase composition of TTCPMF and micTTCPM pastes as prepared and after one year storage at 25 °C was analyzed by X-ray diffraction analysis (Philips X PertPro, using Cu Kα radiation). The surface texture of enamels was observed by a scanning environmental electron microscopy (SEM EVO MA15 (Carl Zeiss, Germany) equipped with EDX/WDX system (Oxford Instruments, United Kingdom) after coating with gold (ion sputter, FINE COAT, Jeol JFC–1100; 1.2 kV, 4 mA for 10 min).

The fluorescent intensity (I_{fluor}) of enamels was observed by the inverted fluorescent optical microscope (Leica DM IL LED equipped with CCD camera) using blue filter (analysis of the difference in fluorescent intensities between sound and treated areas of enamel which allows to consider the degree of enamel demineralization [25, 26] at 100x magnification. The average fluorescent intensities from observed enamel rectangular areas with dimensions 400x400 μm were evaluated by the image analysis (ImageJ8 software). Note that none nonlinear filters were used during the images analysis.

De/remineralization cycling

The 1% solution of citric acid in distilled water at pH 3.6 demineralization phase mimic a typical erosive challenge from acidic drinks (e.g. orange juice) with a similar titratable acidity [27,10]. Specimens were subjected to following de/remineralization protocol for cycling twice a day: firstly, the enamels (n=10 for each group) were subjected to an acid challenge (5 min, 1% w/w anhydrous citric acid in distilled water, pH 3.6 at 37 °C) and rinsed with distilled water; secondly, specimens were brushed with toothpaste slurry (2 min, 1:3 ratio of toothpaste:water) using common Oral B Pro_Health Precision Clean battery brusher (Braun) consequently rinsed with distilled water and dried with filter paper; thirstily, specimens were immersed to remineralization storage solution (137.5 mM NaCl, 3 mM KCl, 0.68mM $CaCl_2$, 7.13 mM K_2HPO_4, 0.5mM Na_2SO_4, 1.5mM $MgCl_2$, 4.2 mM $NaHCO_3$ at pH7, 37 °C) [28] with the concentration of magnesium, calcium and phosphate ions close to artificial saliva [29] for 12 hours. Summary was done 10 cycles before enamel specimens evaluation.

Statistical analysis

One-(testing null hypothesis) and two-way analysis of variance (ANOVA analysis, Statmost software) were used to examine and compare all measured specific properties of enamels ($\alpha < 0.05$). The Kolmogorov-Smirnov test showed that all data were normally distributed. The Student t test (normal distribution) was used to calculate the 95% confidence intervals for mean differences between groups.

RESULTS

The results of individual analysis are shown in Table 1 with statistical one- (null hypothesis) or two-way ANOVA analysis (comparison between groups) (α=0.05). The differences between average surface area roughnesses (ΔS_a) of sound and treated (CaPSi and TTCPMF) enamels were significantly lower than in negative control (storage solution) but no statistically significant differences in ΔS_a were found between fluoride-free groups and control.

Tab.1. Comparison of selected parameters or properties of enamels measured after treatment with various toothpastes and cycling – ΔS_a (difference between surface area roughnesses of sound and treated enamel surfaces), Δh (erosion depth), ΔVMH (surface microhardness recovery), ΔI_{fluor} (differences between means of fluorescent intensities from untreated and treated area of enamels).

	ΔS_a ±SD[nm] n=5	Δh ±SD[μm] n=5	ΔVMH ±SD[%] n=10	Δi_{flour} ±SD* n=10
TTCPM	282±94	6.4±1.8	18.2±8.2 ($p<0.001$)*	4.1±4.2
TTCPMF	183±12	8.3±1.1	-9.8±24.8 (§, $p>0.24$)	5±4.8
micTTCPM	272±85	6.5±2.0	-3.5±30.1 (§, $p>0.72$)	3.2±3.7
CaPSi	191±25	6.8±0.8	0.57±23.4 (§, $p>0.94$)	6.0±4.1
Storage solution	380±46	12.2±1.5	44.7±12.1 ($p<0.001$)*	22.2±6.8
	95% Cl of the difference (significate)			
TTCPM vs TTCPMF	7.43, 193.4 ($p<0.047$)**	-3.91, 0.31 ($p>0.08$)	8.28, 47.54 ($p<0.033$)**	
TTCPM vs storage solution	-200.5, 11.3 ($p>0.07$)	-8.19, -3.49 ($p<0.001$)**	-36.15, -15.58 ($p<0.001$)**	
TTCPMF vs micTTCPM	-157.3, -21.9 ($p<0.05$)**	-0.66, 3.94 ($p>0.12$)	-36.1, 23.5 ($p>0.62$)	
TTCPMF vs storage solution	-248.8, -141.2 ($p<0.001$)**	-5.84, -2.24 ($p<0.002$)**	-73.0, -34.56 ($p<0.001$)**	
micTTCPM vs storage solution	-180.0, -20.8 ($p<0.037$)**	-8.20, -3.16 ($p<0.002$)**	-71.18, -23.8 ($p<0.001$)**	
CaPSi vs storage solution	-238.3, -120.9 ($p<0.001$)**	-7.11, -3.81 ($p<0.001$)**	-62.8, 24.1 ($p<0.001$)**	
TTCPM vs CaPSi	-10.9, 180.9 ($p>0.07$)	-2.37, 1.61 ($p>0.66$)	-1.71, 36.88 ($p<0.04$)**	
TTCPMF vs CaPSi	-45.1, 14.3 ($p>0.54$)	0.13, 2.71 ($p<0.04$)**	-37.98, 17.31 ($p>0.35$)	

* all statistically different from null, $p<0.05$

§ not statistically different from null

** statistically different, $p<0.05$

The addition of NaF to TTCPM (Fig.1a) caused the formation of smoother, a more compact and uniform surface microtexture (Fig.1b). Some microporosity (Fig.1d) with the presence of submicron TiO_2 particles was identified by the point EDX analysis (Fig.2a) on CaPSi treated enamels. In the micTTCPM group (Fig.1c), the fraction of micropores in layer was much higher than in CaPSi group. A high roughness and the strong destruction of enamel structures after acid etching as well as soaking in storage solution only are clearly demonstrated in Figs. 1e.

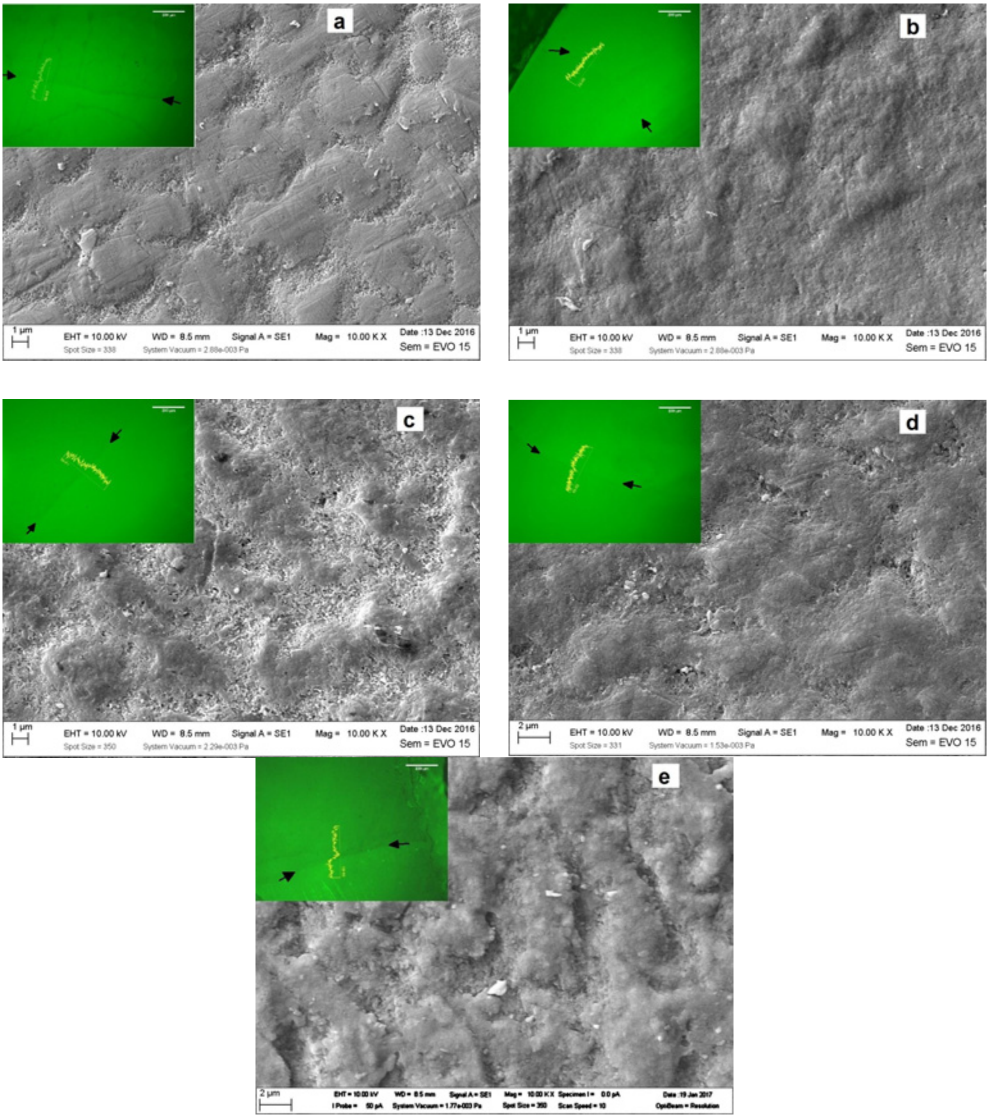

Fig.1. Surface microstructure of enamels after treatment and cycling with TTCPM (a), TTCPMF (b), micTTCPM (c), CaPSi (d) and control (storage solution; e). Fluorescent images from adjacent sound (S) and treated (T) enamels with fluorescent intensity line scan across boundary (arrows) in detail of micrographs.

The EDX analysis of TTCPM and TTPMF coatings verified about 7% rise in the Ca/P ratio while no change in ratio was found on CaPSi treated enamels (a low silica content (Fig.2b) was revealed in coating only). Besides the increase of magnesium content (about double) in all enamel surfaces as compared with sound enamels was confirmed after cycling (Fig.2c,d).

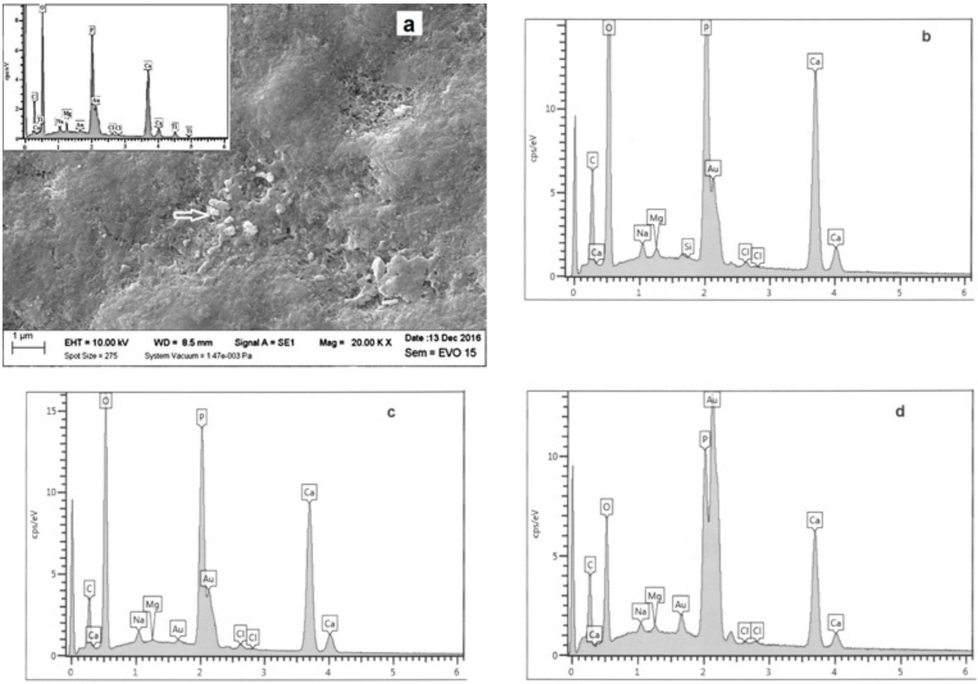

Fig.2. EDX semiquantitative analysis of CaPSi (a- SEM + point EDX analysis of microparticles, b- area EDX microanalysis after cycling) and TTCPMF groups (c – sound enamel, d – after cycling, both analysis from area).

On cross-sections of fractured enamels at higher magnification, the formation of continuous coating composed of very fine precipitates can be visible after cycling (Fig.3a,b).The average coating thickness on enamels of TTCPMF group after soaking in storage solution was almost triple (around 150 nm) than on untreated enamel (about 50 nm).

In the case of Δh, the statistically significant differences ($p<0.05$) were measured between control storage solution group and all paste groups irregardless the type of dentifrice whereas no differences were identified within toothpaste groups. Note that 30-50 % reduction of Δh in dentifrice groups was measured as compared to control.

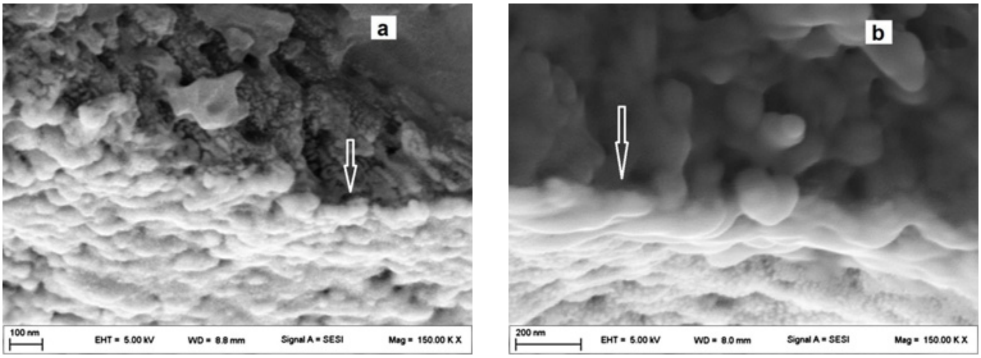

Fig.3. SEM micrographs from cross-sections of teeth with surface protective coating on enamels after cycling (a - control storage solution group; b - TTCPMF group).

About 18% reduction in VHM of TTCP treated enamels after cycling relatively to sound enamel resulted from evaluation of ΔVMH but changes were significantly lower ($p<0.05$) than in control group (storage solution only). No statistically significant differences in ΔVMH were revealed within toothpaste TTCPMF and micTTCPM ($p>0.62$) or CaSiP ($p>0.35$) groups contrary to TTCPM and TTCPMF or CaSiP groups, which were statistically different ($p<0.05$). Null hypothesis for ΔVMH was accepted in the case of TTCPMF, micTTCPM and CaPSi groups, thus, enamels were almost fully remineralized after cycling. The analysis of the fluorescent intensity (Tab.1) of polished sound and treated enamel surfaces (details in Fig.1 show the fluorescent line scan intensities across the boundary between sound and treated enamel surfaces) clearly demonstrates very low differences between the fluorescent intensities and statistically insignificant differences within dentifrice groups what is in accordance with ΔVMH measurements. On the other hand, around 45% reduction in ΔVMH, the decrease in intensity of fluorescence of etched enamel halves as well as more than 30% rise in Δh were identified in negative control group what shows only limited ability of storage solution to enamel remineralization or protection to acid attack. Note that no subsurface enamel lesions were observed by the fluorescent method (direct fluorescence of enamels or after diffusion of rhodamine B to enamel structures) on the cross sections of enamels after cycling.

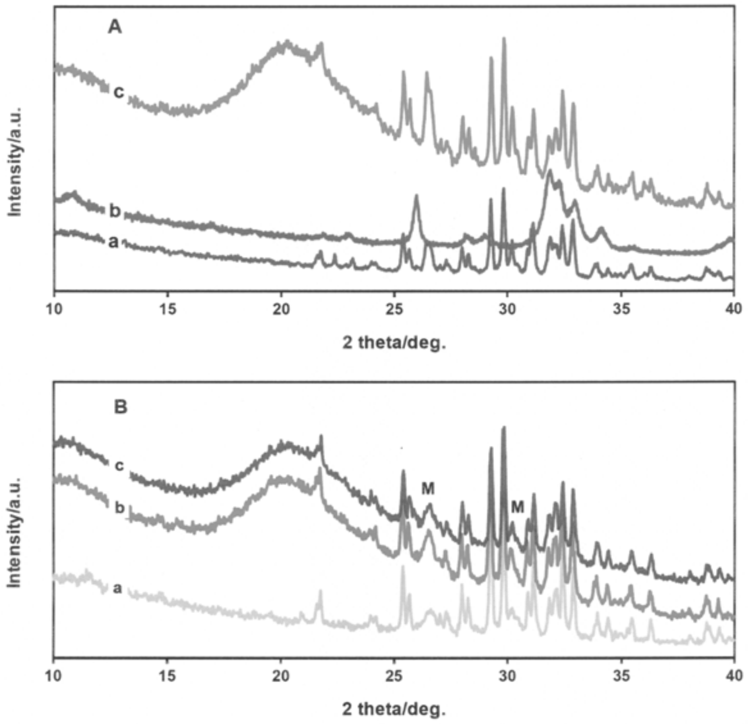

Fig.4. XRD patterns of micTTCPM (A) and TTCPM, TTCPMF (B) toothpastes after one year from preparation stored in closed PP vials (A: a – micTTCPM powder mixture, b – nanohydroxyapatite, c – micTTCPM toothpaste; B: a- tetracalcium phosphate/nanomonetite powder mixture, b – TTCPM toothpaste, c- TTCPMF toothpaste; M-monetite).

The chemical stability of tetracalcium phosphate/monetite mixture in toothpastes during one year storage is demonstrated in Fig.4. No additional lines from new phases like e.g. brushite or hydroxyapatite created by transformation of dentifrice components were found in XRD patterns after storage period. From comparison of XRD patterns of the micTTCPM powder component (Fig.4a) with TTCPMF mixture (Fig.4b) resulted a more crystalline character of monetite (JCPDS 09-0080) in micTTCPM because of the higher intensity of lines and visible splitting of narrowed lines from reflections of (002) and (-220) monetite planes at 2θ ~ 26.5°. The broad XRD line in patterns of toothpastes around 2θ ~ 20° arises from nanocrystalline silica as one of toothpaste components.

DISCUSSION

The commercial TEETHMATE® desensitizer has been studied as dentin desensitizer and the effective tool in preventing demineralization of root dentin but application in the form of slurry showed the insufficient formation of precipitates and incomplete porous coverage of dentin surface [23]. The tetracalcium phosphate/monetite mixtures represent well known biocement self-setting basis developed for bone defect healing with the fast hydrolysis especially the tetracalcium phosphate in aqueous media (with the formation of calcium hydroxide) followed the acido-basic reaction with acid component (monetite) in mixture. The final product of their mutual interaction is the fine nanocrystalline calcium deficient hydroxyapatite [24, 30]. The utilization of this mixture in dentifrices had several advantages e.g. the rapid rise in pH of surrounding, the increase in calcium and phosphate concentrations during brushing with possibility of the rapid nucleation or precipitation of hydroxyapatite on enamel. The rate of cement component transformation due to above described processes depends on physico-chemical properties of phases, appropriate Ca/P ratio and the particle size distribution of powder calcium phosphates as well as on the presence of other chemically active ingredients in toothpastes. Note that the water content in TTCPM dentifrices is critical parameter for achievement of the long-term stability of calcium phosphates during storage in dentifrices and has to be optimized. On the other hand, it is appropriate to admix a small water amount to toothpaste for the partial gelation of some additives (CMC, carrageenan) and enhancing the solubility for example xylitol (or taste ingredients, preservatives, detergents etc.). As resulted from XRD analysis, no lines from nanocrystalline hydroxyapatite phase were identified in XRD patterns of dentifrices after one year storage. This fact verifies that the composition of dentifrices was proper in relation to their stability at used water content.

Fluorides are another anti-caries active components in dentifrices with generally accepted at concentration between 1100-1450 ppm F^- and this amount was added to TTCPMF dentifrice as NaF. Note that NaF was re-precipitated before toothpaste preparation for reduction of the average particle size to submicron dimensions that enhancing the solubility and reactivity of fluorides in a short time after application of TTCPMF toothpaste with a more active calcium phosphate mixture. The surface roughness of enamel is interesting parameter not only for the aesthetic reasons but also for suppression of the bacterial adhesion and subsequent plaque formation in the oral environment. The significant smoothening of enamels treated with fluoride dentifrices was identified which demonstrates the effective influence of fluoride ions on the formation of protective coating despite the fact that no fluorine was found by EDX analysis in layers. Note that detection possibilities of EDX method to determine of low element contents (tenths of wt %) are limited. Contrary to fluorine, the EDX analysis of coatings showed the rapid rise in magnesium content relative to sound enamels which confirms the precipitation of extremely fine calcium and magnesium phosphates (observed by SEM) originating from the storage solution. It is well known the ability of artificial or natural saliva to partial remineralization of enamel [29, 31, 32] in dependence on the actual supersaturation of saliva to hydroxyapatite according to surrounding conditions. The calcium phosphate based pastes like ACP, CPP-ACPF and especially fTCP had a strong effect on reduction of the surface roughness and improving the enamel acid-resistance [4, 33]. The 10% content of nanohydroxyapatite represented the optimal amount of nanohydroxyapatite to direct filling up demineralized enamel in defects and micropores. These adhered particles act as a template on enamel for following precipitation process in remineralization solution and promote growth of hydroxyapatite particles [20, 21]. Similar approximately 15 wt% content of the calcium phosphates was used in TTCPM dentifrices but their remineralization potential was significantly enhanced as compared with above works. The precipitation of hydroxyapatite in the form of fine deposits can be enhanced in the presence of fluoride ions because the fluoroapatite created by the substitution of fluoride ions for OH^- in hydroxyapatite lattice has a lower solubility constant. Thus the higher degree of supersaturation can be achieved in saliva. These conditions conditions allow production of the higher number of nuclei or precipitates which are more uniformly distributed on enamel surface during a short time period after dentifrice application. It is clear that the precipitation of a new phase starts on enamel sites at which the chemical activity was enhanced by the chemical etching. The partial dissolution of hydroxyapatite in starting demineralization step opens the enamel structure with rise in active surface area to remineralization by any external sources of calcium and phosphates. The enhanced number of fine deposites due to faster release of highly active ions from the TTCPMF toothpaste during brushing was responsible for a more intense precipitation of calcium phosphate layer on enamels and reduction in the surface roughness of coatings. On the other hand, micTTCPM group showed better remineralization properties than TTCPM group. The coating in micTTCPM group had a higher porosity which demonstrates nonuniform heterogeneous precipitation of hydroxyapatite probably on particles of partially transformed components with the local supersaturation and faster growth due to larger difference between the surface Gibbs free energy of coarser and finer precipitates.The thicker but more porous layer are formed by this process.

No differences in Δh between toothpaste groups were found but the application of dentifrices significantly reduced Δh as compared with control solution group. This shows the direct effect of dentifrices on the formation of a more compact protection coatings in remineralization solution. The comparison of ΔVMH revealed the lowest ability of the TTCPM group to enamel remineralization contrary to other dentifrices with fully remineralized enamel surfaces (null hypothesis) but the decrease in ΔVMH of TTCPM group was much lower than in control (around 40%). The fluorescent method allows to detect and longitudinally monitor the creation of artificial lesions on extracted human teeth relying upon the relationship between enamel fluorescencent intensity and mineralization status[25]. Direct observations of eroded enamels after cycling by the fluorescent optical microscopy demonstrated comparable results like VHM measurements. Thus, no statistically significant differences were identified within individual groups in ΔI_{fluor} . Despite of the small positive differences or decrease in I_{fluor} of treated enamels (null hypothesis were rejected), ΔI_{fluor} were about 3-4 times lower than ΔI_{fluor} of control group. This fact shows a much effective remineralization of enamels after treatment with any of used dentifrices. Above results are in accordance with other published works e.g. the stronger effect of 10% nanohydroxyapatite slurry in saliva on the enamel remineralization than 2% NaF solution [34] or reduction in the microhardness loss of enamel even in mixture of slurry with acid hydrogen peroxide solution.

In conclusion, the new dentifrice with the active tetracalcium phosphate/monetite mixture showed excellent enamel remineralization potential under de/remineralization cycling comparable with commercial calcium silicate/phosphate toothpastes. It was demonstrated that all toothpaste groups much effectively reduced enamel losses and surface roughness with the fully surface microhardness recovery than control solution group and null hypothesis could be rejected. The addition of fluorides in amount of 1450 ppm to TTCPM significantly improved remineralization activity of toothpaste with nanomonetite phase. The results verified long-term stability of prepared dentifrices which could be used in household as current toothpastes.

Acknowledgement

This work was supported by the Slovak Grant Agency of the Ministry of Education of the Slovak Republic and the Slovak Academy of Sciences, Project No. 2/0047/17.

REFERENCES

[1] Li, X., Wang, J., Joiner, A., Chang, J.: J. Dent., vol. 42, 2014, p. 12
[2] Da Camara, DM., Pessan, JP., Francati, TM., Santos Souza, JA., Danelon, M., Delbem, AC.:. J. Dent., vol. 43, 2015, p. 1249
[3] Danelon, M., Pessan, JP., Neto, FNS., De Camargo, ER., Delbem, AC.: J. Dent., vol. 43, 2015, p. 806
[4] Shen, P., Manton, DJ., Cochrane, NJ., Walker, GD., Yuan, Y., Reynolds, C., Reynolds, EC.: J. Dent., vol. 39, 2011, p. 518
[5] Li, J., Xie, X., Wang, Y., Yin, W., Antoun, JS., Farella, M., Mei, L.: J. Dent., vol. 42, 2014, p. 769
[6] Cochrane, NJ., Cai, F., Huq, NL., Burrow, MF., Reynolds, EC.: J. Dent. Res., vol. 89, 2010, 1187
[7] Wang, Y., Li, X., Chang, J., Wu, C., Deng, Y.: J. Dent., vol. 40, 2012, p. 1119
[8] Nidhi, G., Kunwarjeet, S.: J. Pharm. Biomed. Sci., vol. 24, 2012, p. 79
[9] Hannig, M., Hannig, C.: Adv. Dent. Res., vol. 24, 2012, p. 53
[10] Hornby, K., Ricketts, SR., Philpotts, CJ., Joiner, A., Schemehorn, B., Willson, R.: J. Dent., vol.42, 2014, p. 39
[11] Jones, SB., Davies, M., Chapman, N., Willson, R., Hornby, K., Joiner, A., West, NX.: J. Dent., vol. 42, 2014, p. 46
[12] Joiner, A., Schäfer, F., Naeeni, MM., Gupta, AK., Zero, DT.: J. Dent., vol. 42, 2014, p. 53
[13] Sun, Y., Li, X., Deng, Y., Sun, JN., Tao, D., Chen, H., Hu, Q., Liu, R., Liu, W., Feng, X., Wang, J., Carvell, M., Joiner, A.: J. Dent., vol. 42, 2014, p. 30
[14] Zaze, AC., Dias, AP., Amaral, JG., Miyasaki, ML., Sassaki, KT., Delbem, AC.: J. Dent., vol. 42, 2014, p. 1621
[15] De Alencar, CRB., Magalhaes, AC., De Andrade Moreir Machado, MA., De Oliviera, TM., Honorio, HM., Rios, D.: J. Dent., vol. 42, 2014, p. 1502
[16] Mathews, MS., Amaechi, BT., Ramalingam, K., Ccahuana-Vasquez, RA., Chedjieu, IP., Mackey, AC., Karlinsey, RL.: Arch. Oral. Biol., vol. 57, 2012, p. 525
[17] Vanichvatana, S., Auichay, P.: Inter. J. Oral. Sci., vol. 5, 2013, p. 224
[18] Tschoppe, P., Zandim, DL., Martus, P., Kielbassa, AM.: J. Dent., vol. 39, 2011, p. 430
[19] Esteves-Oliveira, M., Santos, NM., Meyer-Lueckel, H., Wierichs, RJ., Rodrigues, JA.: Clin. Oral. Invest., vol. 24, 2017, p. 291
[20] Jiang, T., Ma, X., Wang, Z., Tong, H., Hu, J., Wang, Y.: J. Dent., vol. 36, 2008, p. 907

[21] Huang, SB., Gao, SS., Yu, HY.: Biomed. Mater., vol. 4, 2009, p. 034104
[22] Min, JH., Kwon, HK., Kim, BI.: J. Dent., vol. 39, 2011, p. 629
[23] Lodha, E., Hamba, H., Nakashima, S., Sadr, A., Nikaido, T., Tagami, J.: Eur. J. Oral. Sci., vol. 122, 2014, p. 404
[24] Medvecky, L., Giretova, M., Stulajterova, R., Kasiarova, M.: Biomed. Mater., vol.10, 2015, p. 025006
[25] Pretty, IA., Pender, N., Edgar, WM., Higham, SM.: Eur. J. Orthod., vol. 25, 2003, p. 217
[26] Pretty, IA., Hall, AF., Smith, PW., Edgar, WM., Higham, SM.: Br. Dent. J., vol. 193, 2002, p. 105
[27] Shellis, RP., Ganss, C., Ren, Y., Zero, DT., Lussi, A.: Caries. Res., vol. 45, 2011, p. 69
[28] Niu, LN., Zhang, W., Pashley, DH., Breschi, L., Mao, J., Chen, JH., Tay, FR.: Dent. Mater., vol. 30, 2014, p. 77
[29] Ionta, FQ., Mendonca, FL., De Oliveira, GC., De Alencar, CRB., Honorio, HM., Magalhaes, AC., Rios, D.: J. Dent., vol. 42, 2014, p. 175
[30] Hirayama, S., Takagi, S., Markovic, M., Chow, LC.: J. Res. Natl. Ins.t Stand Technology, vol. 113, 2008, p. 311
[31] Amaechi, BT., Higham, SM.: J. Dent., vol. 29, 2001, p. 371
[32] Larsen, MJ., Pearce, EIF.: Arch. Oral. Biol., vol. 48, 2003, p. 317
[33] Elkassas, D., Arafa, A.: J. Dent., vol. 42, 2014, p. 466
[34] Swarup, JS., Rao, A.: Contemp. Clin. Dent., vol. 3, 2012, p. 433